Numerical modeling of shear stimulation in naturally fractured geothermal reservoirs

Eren Ucar

Thesis for the Degree of Philosophiae Doctor (PhD)
University of Bergen, Norway
2018

UNIVERSITY OF BERGEN

Numerical modeling of shear stimulation in naturally fractured geothermal reservoirs

Eren Ucar

Thesis for the Degree of Philosophiae Doctor (PhD)
at the University of Bergen

2018

Date of defence: 22.03.2018

Year: 2018

Title: Numerical modeling of shear stimulation in naturally fractured geothermal reservoirs

Name: Eren Ucar

Print: Skipnes Kommunikasjon / University of Bergen

Preface

This dissertation is submitted as a partial fulfillment of the requirements for the degree of Doctor Philosophy (Ph.D.) at the University of Bergen. The advisory committee has consisted of Inga Berre (University of Bergen), Eirik Keilegavlen (University of Bergen), and Jan M. Nordbotten (University of Bergen).

The Ph.D. project has been financially supported by the Research Council of Norway through grant 228832/E20.

Acknowledgements

There are many who deserve to be thanked. First of all, I would like to thank my main advisor, Inga Berre, for her excellent supervision, infinite enthusiasm, and constant encouragement. Also, I am sincerely thankful to my co-advisor, Eirik Keilegavlen, for his excellent guidance. His door has always been open. He has always known how I understand and what I need to hear. I am also thankful to Jan Nordbotten for his valuable contributions.

I would like to thank my dear colleagues and the academic staff at the Department of Mathematics, University of Bergen. Carina Bringedal deserves special attention here for her generous support and endless friendship from the beginning of this journey. Also, I consider myself very lucky to share an office with a number of fantastic people, they all deserve special thanks: Alessio Fumagalli, Runar Berge, and Ivar Stefansson. I am also grateful to Wietse Boon and Michael Sargado for their support whenever I needed.

I am thankful to my family, especially to my mother. Annem, teşekkur ederim, sensin benim cesaretim.

Last, but not least, I would like to express my love and gratitude to my husband, Peter Andre Drønen, for his endless love and support. This thesis is one of the many things that we will succeed together. I am the luckiest person on Earth.

Eren

Abstract

Shear-dilation-based hydraulic stimulations are conducted to create enhanced geothermal systems (EGS) from low permeable geothermal reservoirs, which are initially not amenable to energy production. Reservoir stimulations are done by injecting low-pressurized fluid into the naturally fractured formations. The injection aims to activate critically stressed fractures by decreasing frictional strength and ultimately cause a shear failure. The shear failure leads to a permanent permeability enhancement of the fractures, which contributes to the overall reservoir permeability, owing to the damage in fracture surface characteristics during the shear failure. Shear stimulation is considered a key for geothermal energy development; however, seismicity is a critical by-product, which has to be controlled. Numerical modeling can provide a deeper understanding on governing mechanisms, which is essential for reservoir assessments and the control of seismicity. The primary goal of this thesis is to aid further development of EGS by contributing to the current state-of-the-art for numerical modeling of shear-dilation-based hydraulic stimulations.

Numerical modeling of shear-dilation-based hydraulic stimulations requires mathematical modeling of flow and mechanical deformation in fractured formations. The initial focus of the thesis is the modeling of the mechanical deformation of naturally fractured rock. The deformation and stress state of the rock are controlled by the deformation of pre-existing fractures, which is governed by different equations than the deformation of the surrounding formation. A cell-centered finite-volume approach is developed where the fractures are represented as co-dimension one inclusions in the domain. The method is capable of modeling deformation considering open and closed fractures with complex and nonlinear relationships governing the displacements and tractions at the fracture surfaces. The method aims to provide benefits for studies including flow and deformation couplings in a discontinuous rock.

Hydraulic stimulations are essentially coupled hydro-mechanical processes, where the deformation of fractures has an impact on the permeability as well as on the stress state of the rock. We develop a computational model, which has the capability to capture these interrelations in two- or three-dimensional domains. Considering the significance of the pre-existing fractures, we model the reservoir as a network of explicitly represented large-scale fractures immersed in a permeable rock matrix. The model can forecast the permeability evolution of geothermal reservoirs with complex fracture networks.

To be able to mitigate the seismic hazards, the contributing processes and the interaction between them should be examined. The computational model developed here also has the capability to investigate the induced seismicity. By using the developed model, a novel hypothesis regarding the induced seismicity generated after the termination of injections has been tested. During the fluid injections, the pressure builds up inside the fractures, which causes normal deformation and increases the void place between the fracture surfaces. The termination of the injections reverses the void increase; i.e., the fracture starts to close owing to the pressure decrease. We

identify that the fracture closure is one of the mechanisms that are responsible for the induced seismicity generated after the termination of injections.

Outline

This dissertation consists of two parts. The first part contains the background theory covering the papers found in the second part.

Part I is structured as follows: In Chapter 1, enhanced geothermal systems, shear stimulation, induced seismicity, and the modeling challenges of shear stimulation are introduced. The physical processes pertaining to shear stimulation are presented in Chapter 2, and the constitutive relations for fracture deformation are provided in Chapter 3. In Chapter 4, the numerical methods for the processes are presented. Finally, the main findings are discussed, and an outlook is provided in Chapter 5.

The included papers found in Part II are:

Paper A: Ucar, E., Keilegavlen, E., Berre, I., and Nordbotten, J. M. (2016). "A Finite-Volume Discretization for the Deformation of Fractured Media." submitted to *Computational Geosciences*, can be found in *arXiv:1612.06594v2*.

Paper B: Ucar, E., Berre, I., Keilegavlen, E. (2016). "Modelling of the Shear-Dilation-Based Hydraulic Stimulation in Enhanced Geothermal Systems Considering Fractures in Different Scales." in proceedings for the European Geothermal Congress 2016 in Strasbourg, France.

Paper C: Ucar, E., Berre, I., Keilegavlen, E. (2017). "Three-Dimensional Numerical Modeling of Shear Stimulation of Naturally Fractured Reservoirs." submitted to *Journal of Geophysical Research-Solid Earth*, can be found in *arXiv: 1709.01847*.

Paper D: Ucar, E., Berre, I., Keilegavlen, E. (2017). "Postinjection Normal Closure of Fractures as a Mechanism for Induced Seismicity." *Geophysical Research Letters, 44*, 9598–9606. doi:10.1002/2017GL074282

Contents

Part I

Background

1. Introduction

Geothermal energy is the thermal energy that is generated and stored in the Earth's crust. Heat flows through the crust of the Earth due to two primary processes: heat generated by the decay of radioactive elements in the crust and continuous heat transfer (both conduction and convection) from Earth's molten metal core [60; 87; 106]. Harnessing geothermal energy for industrial purposes was started in the early 20th century, and it is reported that the major geothermal power potential remains untapped [74; 96].

Using renewable energy sources has become a necessity rather than an option due to the negative economic and environmental impacts of heavy reliance on fossil fuels. Currently, 23.5 % of the global electricity generation is provided by renewable energy sources, which are dominated by hydropower (17.2 %) and wind (3.5 %). Geothermal energy is seen as a complement to other renewable energy sources because it can provide continuous baseload power generation with a small footprint and minimum environmental impacts [106]. These attributes of geothermal energy combined with its widespread distribution and no storage requirements make the geothermal energy one of the most promising and clean energy resources in the world [106]. Geothermal energy gains significant momentum as there has been a spike in geothermal projects worldwide; a total of 44 new geothermal power projects began development throughout 23 countries between March and September 2016, which is more than the annual development over the previous two years [11]. Despite its advantages and recent project developments, the current geothermal energy share in global electricity generation is still limited to 0.3 % [55]. The current production is mainly provided from hydrothermal and magmatic systems where hot fluids are extracted from naturally permeable reservoirs located in shallow (0 - 0.1 km) or intermediate depths (0.1 - 4 km) [43]. Bertani [20] reports that 8.3% of global electricity need can be supplied from geothermal sources by 2050. However, to make the geothermal energy a major supplier to the global energy need, the geothermal energy that is confined to the greater depths (> 4 km) should be exploited [87].

Deep geothermal sources have high potential for electricity generation owing to their high temperatures. However, high formation temperature should be accompanied by sufficient amount of fluid to carry heat from the reservoir and high formation permeability to transport the fluid at a high flow rate. Although high temperature can be found extensively, natural permeability levels and the amount of existing fluid do not generally meet the criteria for viable production rates. A remedy is to create artificial reservoirs by enhancing (or engineering) the geothermal systems.

1.1 Enhanced geothermal systems

The common formations observed in deep geothermal reservoirs, such as crystalline igneous rocks, preserves inherently very low natural porosity and permeability [106].

The low permeability limits the hydraulic connection between the production/injection wells and the fractured reservoir, which leads to inefficient production rates. Enhanced geothermal systems (EGS) aim to cure this limitation by mainly three stimulation methods: thermal, chemical and hydraulic stimulation [25]. Thermal stimulation is conducted by cold-water injections, which cause contraction of rock and consequent expansion of fractures [45; 49]. Chemical stimulation (a.k.a. acidizing) is based on acid injection into the formation with the aim of permeability enhancement through transport and precipitation processes [91]. Another common stimulation method is hydraulic stimulation, which is performed by injecting pressurized fluid into the formation. Hydraulic stimulation has the potential to stimulate larger regions than chemical and thermal stimulations, whose effects are localized to the proximity of wells. In this thesis, we focus on hydraulic stimulations.

Depending on the injection pressure and the stress state of the reservoir, three common mechanisms can be encountered during hydraulic stimulations in EGS. Tensile fractures can be initiated (hydraulic fracturing), the shear strength of the fractures can be decreased causing shear and normal deformations on the fracture surfaces (shear stimulation), and mixed-mechanism can occur in which opening and shearing of fractures take place simultaneously. The conventional hydraulic fracturing method has been applied widely in the oil and gas industry from the late 1940s [63], and the method has been adapted to geothermal applications [69; 116]. The success of the hydraulic fracturing has been lower than expected especially when applied to the naturally fractured reservoirs. The possible reasons of inefficient fracturing are listed as high pressurization related fluid leak-off acceleration to the outside of the wellbore area, fracture initiation at non-preferred locations, and inefficient proppant transport [54; 93; 110; 111]. Moreover, public concerns regarding hydraulic fracturing and the use of certain chemical substances give rise to groundwater and air contamination discussions [28]. Thus, the investigation of alternative stimulation strategies is recommended [111], and shear-dilation-based hydraulic stimulation (a. k. a. shear stimulation, low-pressure stimulation or hydroshearing), is discussed as a possible remedy [81; 89; 93].

1.2 Shear-dilation-based hydraulic stimulation

Shear-dilation-based hydraulic stimulations are suggested for formations which are subjected to high deviatoric stresses [81; 89]. High deviatoric stresses (which means a big difference between the maximum and minimum principal stresses) promote the existence of critically stressed fractures (favorably oriented fractures) such that these fractures exposed to high shear forces and can be activated by low-pressure fluid injections. As with the hydraulic fracturing, shear stimulations are also conducted by fluid injections; however, the pressure level is intentionally kept below the minimum principal stress not to cause tensile fractures. The low-pressure injections cause stress alterations on the fractures, which decrease the frictional strength of the fracture surfaces, eventually leading to shear movements of two rough surfaces of fractures. During the shear deformation, the asperity movement between fracture surfaces

causes dilation between them, which provides additional void space for fluid flow as shown in Figure 1.1. Unlike the hydraulic fracturing, shear stimulation does not require proppant injections (or requires very little). The permeability enhancement provided by shear dilation is assumed to be irreversible because of the irregularity and roughness of the fracture surface [92; 93]. An illustration of the shear stimulation in EGS is provided in Figure 1.2.

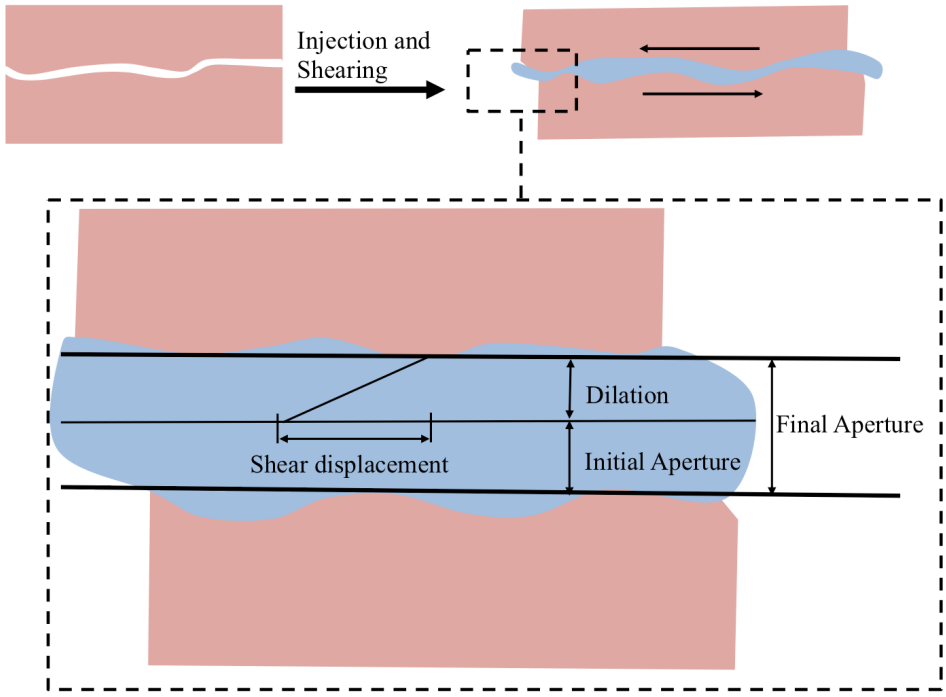

Figure 1.1: Induced shear movement and corresponding dilation (reproduced from [93]). (Upper) Fluid injection creates an offset between fracture surfaces. (Lower) A closer look at the dashed area. The dilation is the cause of permeability enhancement.

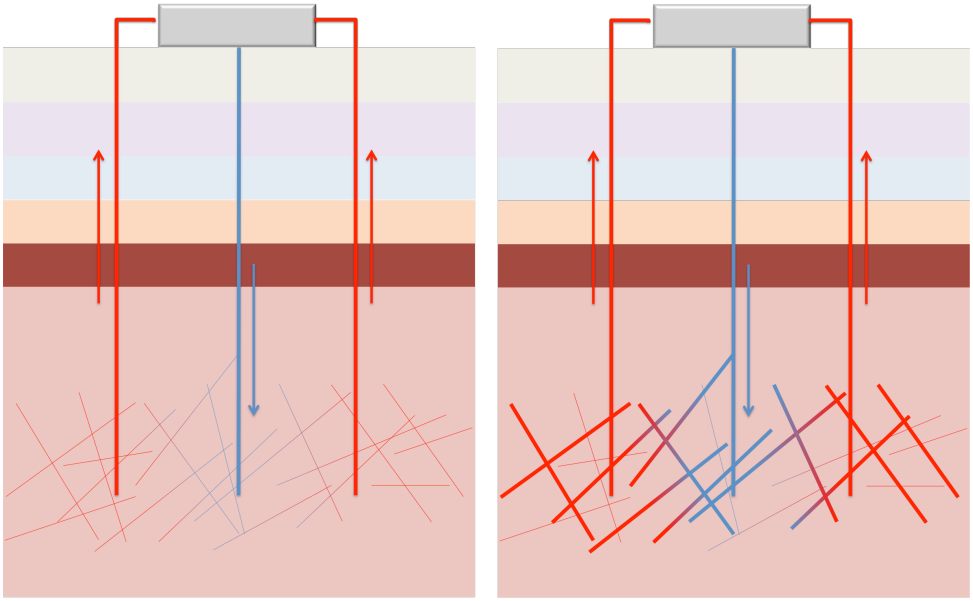

Figure 1.2: A reservoir (left) before and (right) after the stimulation. Shear stimulation increases the permeability of favorably oriented fractures. The permeability of the fractures is visualized by the thickness of the lines. The cold fluid is injected (shown with blue) and traveled in fractures where the reservoir works as a heat exchanger. The hot fluid (shown with red) is produced from production wells.

1.3 Induced seismicity

Seismicity is deliberately induced in EGS applications to engineer the geothermal reservoirs that have poor initial permeability. A major challenge of hydraulic stimulations is the control of induced seismicity [30; 73]. In fact, induced seismicity is considered as a possible hazard for several kinds of subsurface applications including mining, oil and gas hydraulic fracturing, extraction of natural gas and disposal of wastewater by injection [40; 41; 46; 53; 108]. The Earth's crust generally supports high shear stress levels and is often close to shear failure; therefore, small perturbations during any subsurface applications can affect fracture stability and trigger earthquakes [40; 41].

A fracture located in the subsurface is under shear and normal stresses caused by the tectonic stresses such as the weight of earth and the stresses caused by plate motions [24; 75; 107]. Following the classical theory of friction, the fracture, which can be thought of as a plane of weakness, will remain locked as long as the applied shear stress is less than the frictional strength of the fracture surface contacts [40]. The main shear failure mechanisms associated with establishing and operating EGS can be listed as (i) reduction of the frictional strength by the pore pressure increase via

fluid injection (ii) reduction of the frictional strength due to the contraction of rock formations via cold fluid injection (iii) perturbation in the stress state by volume change due to fluid withdrawal/injection (iv) perturbation in the characteristics of the fracture surfaces via chemical processes [73]. The primary focus of this thesis regarding induced seismicity mechanisms is the reduction of the frictional strength by the pressure increase via fluid injections.

The induced seismicity associated with EGS has been observed to be minor concerning damage and magnitude [50]; however, the seismic events can still be felt as many EGS are located in near proximity to communities for the efficient use of geothermal energy. Despite its low magnitude nature, the public tolerance to induced seismicity is delicate due to the fears of, for instance, the small events possibly being precursors of larger ones or possible structural damage similar to that caused by large natural earthquakes. In order to avoid intolerable induced seismicity, a reactive control approach, which is called traffic-light system, is applied for several EGS applications [22; 51; 73]. The traffic-light system can be briefly explained as the ongoing geothermal operation, such as stimulation, has to be altered/adjusted whenever a pre-defined threshold of one indicator of seismic hazard is reached [22]. This protocol has been considered to be too simplistic, especially for the case of the Deep Heat Mining project in Basel, where the termination of injection did not prevent the occurrence of the publicly felt seismic event. In Basel, a relatively high level of seismicity was observed on 8 December 2006 during hydraulic stimulations, and the injection was first decreased and then terminated to prevent the occurrence of larger seismic events. However, more substantial seismicity occurred 4 hours after the termination of injection. The following three months, several events were still observed in the area. The Basel project eventually was shut down permanently due to public reaction and the damage allegedly caused by the induced seismic events [35]. As another example, the traffic light system would have also been insufficient if implemented to the Soultz-sous-Forêts geothermal power plant during the major stimulations of 2003 in which large induced seismicity occurred several days after the fluid injection was terminated [39].

The above-mentioned past events underline that the mechanisms of the induced seismicity are not adequately handled with the traffic-light systems, and a deeper understanding of the physical processes associated with induced seismicity is required to implement a large-scale application of the EGS technology [73]. To that end, there have been several attempts to diagnose mechanisms leading to induced seismicity [12; 26; 65; 76; 77; 97].

1.4 Challenges in modeling and simulation of hydraulic stimulation

Mathematical modeling plays a key role in the reservoir assessment for EGS applications. Direct observations of reservoir behavior are not possible since the permeability enhancements and induced seismicity take place deep in the crust. In

addition, field experiments with samples in large scales are technically challenging and costly. Although measurements from fields such as well logs and microseismicity recordings provide essential information, they possess incompleteness and uncertainty [51; 102]. Therefore, the field data should be accompanied by numerical models for reservoir assessment. Numerical studies represent the governing mechanisms in an approximate manner, allow to qualify the essential mechanisms and forecast the outcomes of stimulations in a large variety of settings. The objective of this thesis is to contribute to the current state-of-the-art for numerical modeling of the shear-dilation process. We construct our studies to serve the theoretical challenges of stimulation modeling and the conceptual challenge of induced seismicity in EGS.

The first challenge that is targeted here is incorporating the discontinuous and complex nature of rocks into the modeling. The existence of fractures modifies the mechanical and hydraulic properties of the rock mass significantly. In a mechanical sense, fractures have more compliant nature than the rock, and in a hydraulic sense, they have higher permeability than the rock. Given the importance of the fractured rock behavior, the first contribution of this thesis is:

1. **Formulating a cell-centered discretization method for mechanical deformation modeling of fractured formations**. In Paper A, an existing cell-centered discretization method for elastic deformation in porous media is upgraded as the effect of fractures to rock deformation is captured by modeling them as co-dimension one inclusions in the domain. The developed method is capable of modeling deformation considering open and closed fractures with complex and nonlinear relationships governing the displacements and tractions at the fracture surfaces. The method serves as an important tool for modeling studies that include coupling of flow and mechanical deformation because it shares the same data structure with commonly used cell-centered flow discretization method in porous media. The developed method provides a door for conducting accurate modeling studies with the explicit representation of fractures.

The second challenge that is targeted here pertains to hydraulic stimulation modeling as several physical processes take place at the same time during the stimulations. Mathematical formulation of the final reservoir stimulation model requires coupling of a number of physics such as multiphase fluid flow, mechanical deformation, fracture deformation, heat transfer, and chemical processes. These processes are represented by a set of nonlinear or linear equations that are dominated by pre-existing fractures, which may have a variety of orientations and scales. In this setting, the second contribution is:

2. **Developing a computational model for shear stimulation with representing pre-existing fractures in different scales and orientations.** In Papers B and C, we present our method, which couples fluid flow in both rock matrix and fractures with linear deformation of rock matrix and non-linear deformation of fractures. The initial version of the method, which is presented

in Paper B, is used for the simulation of shear stimulation in a 2D synthetic reservoir. In Paper C, the method is applied to two cases in which a synthetic 3D geothermal reservoir that hosts 20 fractures with distinctive orientations and properties is stimulated. The cases are discussed under the topic of permeability enhancement, induced seismicity, and the significance of rock matrix permeability. Our method aims to assist geothermal reservoir assessments by, for example, simulations of different injection scenarios (e.g., monotonic, cyclic, rate-controlled, pressure-controlled injection) for reservoirs structurally dominated by complex fracture networks.

Mitigation of large induced seismicity, as presented in Section 1.3, has vital importance for the full development of EGS. Deep understanding of physical processes of induced seismicity serves as a tool for avoiding a seismic hazard. Thus, the third contribution is:

3. **Identifying fracture closure as a mechanism for postinjection seismicity.** Paper D tests a novel hypothesis pertaining to the mechanisms underlying elevated postinjection events occurring at the boundaries of the stimulation regions by using the computational method developed in Paper C. The hypothesis originates from the elastic normal deformation of the fractures due to the pressure decrease following the termination of injection. The normal deformation decreases fracture void space to host the fluid, which pushes the pressure propagation away from the injection region and increases the potential for postinjection seismicity at the outer rim of the previously active seismic region. The hypothesis is verified by numerical experiments, which are conducted in 3D formations with simple and complex fracture networks.

2. Coupled processes in fractured formations

Subsurface rock has a special nature, and perhaps the most realistic description of this nature would be discontinuous, anisotropic, inhomogeneous, and non-elastic material [59]. This particular nature of rock combined with the number of processes taking place during any engineering operation challenge the modeling studies significantly. Although the recent rapid progress in computer technology has helped the tackling of these problems greatly, modeling simplifications are still inevitable. This chapter starts with the brief description of subsurface fractured rock and continues with summaries of the typical modeling simplifications.

The governing processes of flow, transport, and deformation in fractured formations have been appealing subjects in the literature from the late 1980s due to their essential role in many engineering fields such as underground radioactive waste repositories, contaminant transport analysis, and gas/oil recovery [59]. One can count fluid flow, rock mechanics, and heat transfer as the primary processes and these processes may interact with each other, i.e., the processes are characterized as coupled. In fact, not only these three but also chemical processes can be included in the set of coupled processes, but we do not focus on the latter here. Thus, the chapter presents the governing equations for fluid flow, rock mechanics, and heat transfer, which are structured with the common assumption of rock masses being a porous material [57]. For a rock mass where the pore space is filled with fluids under pressure, the connection between pore pressure and stress state of the rock can be profoundly linked to the failure of fractured formations. Therefore, we close the chapter with a brief description of poroelastic relations.

2.1 Naturally fractured rock

Fractures are the most common type of geological structure which divide the rock masses into the blocks [57]. The existence of fractures alters the physical properties of rock masses significantly. Especially for hard crystalline rocks, fractures dominate several processes due to their high permeability and deformation tendency.

Fractures can be characterized as joints according to their offset between surfaces, that is, a joint can be named as a fracture if the fracture surfaces exhibit a relative displacement [57]. However, in this thesis and the attached papers, fractures represent any form of discontinuities that exist in the rock mass.

In this thesis, the rock is modeled as a porous material that hosts pre-existing fractures. Moreover, we consider the fact that the fractures in the rock can be observed at all scales and this heterogeneity should be preserved. Although fractures have great geometrical complexity in reality, the pre-existing fractures are assumed to consist of two planar surfaces, and the geometrical complexity of the fracture walls is accounted in a simplified manner (discussed in Chapter 3). Notably, the rock masses

surrounding the fractures (the porous material) are named as the rock matrix throughout this thesis for clarity.

2.2 Modeling approaches for fractured rock

Modeling of the physical processes can be a challenging problem because of the structurally complicated geometry of the reservoir. The complexity of the problem often restricts researchers to consider simple models for fractured geometries. Here, we briefly present three conceptual models for fractured formations: continuum models, the discrete fracture network (DFN) approach, and the discrete fracture-matrix (DFM) approach.

2.2.1 Continuum models

Continuum models are widely employed for large-scale analyses, where the rock matrix and pre-existing fractures are treated as equivalent continua. The behavior of the rock mass that hosts many fractures is governed by equivalent properties established by a homogenization/upscaling process [56; 58; 112]. A fractured rock, represented by a continuum approach should present a limited number of regions, each having uniform physical properties. Continuum models are preferable especially for large-scale analysis of rock masses with dense fracture networks because the explicit representation of each fracture in the network would be computationally very intensive (Figure 2.1a). Poorly connected fracture networks are also suitable to be treated with a continuum description (Figure 2.1b). The main drawback of this method is the elimination of discrete effects of the fractures, which could be essential in the context of hydraulic stimulation.

2.2.2 Discrete fracture network (DFN) model

DFN model is another common approach [12; 26; 77]. In DFM model, the reservoir is treated as a combination of distinct, individual fractures and impermeable rock matrix. DFN approach is most useful for modeling of large-scale fracture network that dominates the system, and when an equivalent continuum model is difficult to establish (Figure 2.1c). DFN model is a powerful tool due to its advantage of capturing the distinct effects of fractures but more computationally intensive than the continuum models. This approach suffers from the heterogeneous structure of the fractured rock especially when the time scale of the problem is long enough such that matrix diffusion cannot be ignored. When the fractures exist in various forms of sizes, locations, and orientations; the explicit representation of large numbers of fractures makes the computational model less efficient. In addition, all fractures that contribute to flow typically cannot be represented in the model. Alternatively, the fine-scale heterogeneity can be eliminated to improve the computational time, which may affect the predictions of hydraulic stimulation severely.

2.2.3 Discrete fracture-matrix (DFM) model

DFM approach has emerged as an alternative method for accurate modeling of fractured formations that have fractures in different scales (Figure 2.1d). DFM model can be thought of as a combination of continuum approach and DFN model. In this model, the fractures are generally divided into two categories: large-scale fractures and fine-scale fractures. The effects of the fractures are computed in a hierarchical manner; the large-scale fractures, which contribute to the governing processes, are represented explicitly, and the effect of the fine-scale fractures and the porous media is captured implicitly via upscaling them into continua. DFM models (also sometimes named as hybrid models [68]) are successfully applied in several studies [42; 61; 68; 101]; however, they can be applied for analysis of smaller scale domains because of their higher computational cost than continuum and DFN models.

In this thesis, the rock is assumed to have fractures in various scales; thus, we apply a DFM approach to model fractured formations such that the corresponding heterogeneity can be preserved.

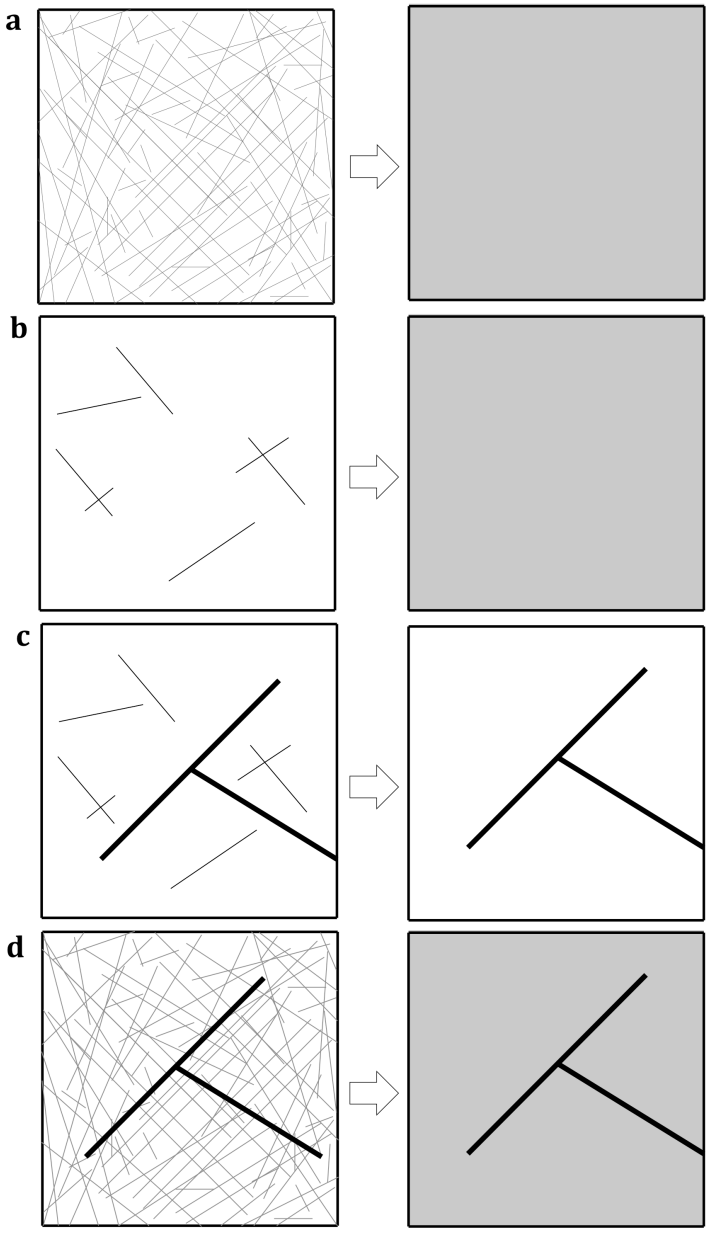

Figure 2.1: Modeling approaches for fractured rock. (a) A high-density fracture network example to be represented as a continuum (b) A poorly connected fracture network example to be represented as a continuum (c) A suitable rock structure for DFN type of modeling (d) A suitable rock structure for DFM type of modeling.

2.3 Fluid flow in fractured rock

The fluid flow is governed by the principle of mass balance. For a single-phase and isothermal flow, the conservation of mass equation is:

$$\phi c_f \frac{\partial p}{\partial t} + \nabla \cdot \boldsymbol{w} = q, \tag{2.1}$$

where ϕ is porosity of solid material, c_f is the compressibility of the fluid, t is time, p is pressure, $\boldsymbol{w}$ is Darcy velocity, and q is a source term. Neglecting gravitational effects, the Darcy velocity can be written as

$$\boldsymbol{w} = -\frac{\boldsymbol{K}}{\eta} \nabla p, \tag{2.2}$$

where $\boldsymbol{K}$ is the intrinsic permeability of the solid material and η is the fluid viscosity. $\boldsymbol{K}$ should be defined as a second order tensor for an anisotropic medium or scalar value for isotropic medium.

Keeping in mind the DFM approach where the fluid flow can take place both in the rock matrix and in fractures, the material properties of the solid material, porosity, ϕ, in equation (2.1) and the permeability, $\boldsymbol{K}$, in equation (2.2), should be customized according to the rock matrix and the fractures. For the rock matrix, the porosity is considered to be a constant value, for example, a value between 0.18 and 1 for granite [109]. The porosity of fractures can also be constant or can be related to the aperture of fractures as noted in Paper C. Regarding the permeability values, the rock matrix has been considered as a material that preserves smaller permeability than the fracture. For the calculation of flow in the fractures, $\boldsymbol{K}$ in the equation (2.2) should be defined with the fracture permeability, K_f, as $\boldsymbol{K} = K_f \boldsymbol{I}$. K_f can be calculated by the common approximation of fluid flow in fractures as Poiseuille flow between parallel plates, namely the cubic law,

$$K_f = \frac{e^2}{12}, \tag{2.3}$$

where e is the hydraulic aperture of fractures [57].

2.4 Rock mechanics

The change in the stress field of the rock is obtained by the principle of momentum balance and constitutive equations for the different rocks in the reservoir. One of the most common constitutive relations for a rock matrix, especially for hard rocks, is Hooke's law with elastic behavior [57; 59].

Ignoring the body forces and assuming quasi-static condition, the momentum balance reads

$$\nabla \cdot \boldsymbol{\sigma} + \boldsymbol{f} = 0, \tag{2.4}$$

where $\boldsymbol{\sigma}$ is Cauchy stress tensor and $\boldsymbol{f}$ is the body force vector. The stress tensor, $\boldsymbol{\sigma}$, describes any stress field is of the form

$$\boldsymbol{\sigma} = \begin{pmatrix} \sigma_{xx} & \tau_{xy} & \tau_{xz} \\ \tau_{xy} & \sigma_{yy} & \tau_{yz} \\ \tau_{xz} & \tau_{yz} & \sigma_{zz} \end{pmatrix}. \tag{2.5}$$

The traction vector, $\boldsymbol{T}(\boldsymbol{n})$, on an arbitrary plane whose unit normal vector is $\boldsymbol{n} = (n_x, n_y, n_z)$ can be calculated by

$$\boldsymbol{T}(\boldsymbol{n}) = \boldsymbol{\sigma} \cdot \boldsymbol{n}. \tag{2.6}$$

Any deformation in the rock is quantified by the deformation vector, $\boldsymbol{u}$, which is the change in the position of a given particle of rock. Under the small-strain assumption, the linearized strains, $\boldsymbol{\varepsilon}$, are defined as the symmetric part of the displacement gradient:

$$\boldsymbol{\varepsilon} = \frac{\left(\nabla \boldsymbol{u} + (\nabla \boldsymbol{u}^T)\right)}{2}. \tag{2.7}$$

Hooke's Law states that the components of the strain tensor are linearly related to the components of the stress tensor:

$$\boldsymbol{\sigma} = \mathbb{C} : \boldsymbol{\varepsilon}, \tag{2.8}$$

where $\mathbb{C}$ is fourth-order tensor that defines the stiffness of the material. Equation (2.8) can be rewritten as

$$\boldsymbol{\sigma} = 2G\boldsymbol{\varepsilon} + \lambda\, tr(\boldsymbol{\varepsilon})\, \boldsymbol{I}, \tag{2.9}$$

for an isotropic medium where G and λ are the Lamé constants, G being the shear modulus. The equations given in this section only cover the mechanics of the rock matrix surrounding the fractures.

The mechanical behavior of the fractures is different from the rock matrix. The stress alterations caused by fracture deformation are spatially heterogeneous, and interactions of neighboring fractures are dependent on their relative orientations and locations. Thus, the constitutive equations regarding the deformation of pre-existing fractures and the effects on rock matrix deformation are not given here. Instead, the whole Chapter 3 is devoted to the fracture deformations.

2.5 Heat transfer in fractured rock

The hydraulic stimulation model developed in this thesis does not include thermal effects, i.e., the reservoir temperature is assumed to be constant during the

stimulation. However, the effect of the stimulation process is illustrated by simulation of tentative reservoir production scenarios in Paper C. Therefore; the heat transfer equation is presented for the sake of completeness.

The heat transport equation is obtained by the principle of energy conservation under the assumptions of incompressible fluid without any phase change and incompressible rock matrix. We also assume that there is a local thermodynamic equilibrium between rock matrix and fluid. Then, the heat transfer equation reads:

$$\rho_{eff} c_{p,eff} \frac{\partial \theta}{\partial t} + \rho_f c_{p,f} \boldsymbol{w} \cdot \nabla \theta - \nabla \cdot \left(\boldsymbol{\kappa}_{eff} \nabla \theta \right) = h_{eff,} \tag{2.10}$$

where θ stands for both fluid and rock matrix temperature due to the local equilibrium assumption. Here, the effective heat capacity per volume, $\rho_{eff} c_{p,eff}$, effective thermal conductivity, $\boldsymbol{\kappa}_{eff}$, and total heat sources, h_{eff}, are given by

$$\begin{aligned} \rho_{eff} c_{p,eff} &= (1-\phi)\rho_r c_{p,r} + \phi \rho_f c_{p,f}, \\ \boldsymbol{\kappa}_{eff} &= (1-\phi)\boldsymbol{\kappa}_r + \phi \boldsymbol{\kappa}_f, \\ h_{eff} &= h_r + h_f, \end{aligned} \tag{2.11}$$

where ρ_f is fluid density, ρ_r is density of rock matrix, $c_{p,r}$ is heat capacity of rock matrix, $c_{p,f}$ is heat capacity of fluid, $\boldsymbol{\kappa}_r$ and $\boldsymbol{\kappa}_f$ are the thermal conductivities of rock and fluid, and h_r and h_f are heat source terms for the rock matrix and the fluid phase, respectively. In equation (2.10), the time dependent term is known as the storage term, the velocity dependent term is the advective term, $\mathcal{H}^{adv}$, and the third term is the diffusion term, $\mathcal{H}^{diff}$.

In Paper C, a production scenario is created to illustrate the effect of shear stimulation to the reservoir. In this scenario, the temperature distribution of an artificial reservoir after one year of production is illustrated by solving equation (2.10) with (2.11).

2.6 Poroelasticity

Following or prior to the fluid injection, the pore space of the rock mass is filled with fluids under pressure. The pore pressure acts outward from the pore space, in some sense acts as a tensile force. This behavior initially characterized by the concept of 'effective stress' by Karl von Terzaghi [105]. According to Terzaghi, the failure of a solid is controlled by the effective stress, which is defined as

$$\sigma_{1,eff} = \sigma_1 - p, \sigma_{2,eff} = \sigma_2 - p, \sigma_{3,eff} = \sigma_3 - p, \tag{2.12}$$

where σ_1, σ_2, σ_3 are the principal stresses defined positive for compression. Terzaghi's theory is followed by a phenomenological approach of poroelasticity, Biot's theory of isothermal consolidation of elastic porous media [21]. According to

Biot's theory of poroelasticity, the relation of stress to deformation and pore pressure for a linear isotropic poroelastic medium is given by

$$\boldsymbol{\sigma} = \mathbb{C}: \boldsymbol{\varepsilon} - \alpha p \boldsymbol{I}, \tag{2.13}$$

where α is Biot's coupling coefficient which is also known as the effective stress coefficient. Fluid injection can create variation in the volume of the rock matrix and pore space, and the change in the volume of rock matrix can affect the stress-state of the rock. This is described by

$$\frac{1}{\rho_{f,0}}(m - m_0) = \alpha \varepsilon_v + \frac{1}{M}(p - p_0), \tag{2.14}$$

where subscript 0 refers to the reference state, m is the fluid mass per unit bulk volume, ε_v is the volumetric strain (trace of the strain tensor), M is the Biot modulus [31].

Although poroelasticity and thermoelasticity are important topics for subsurface applications, they are commonly ignored for modeling studies regarding hard rocks [26; 52; 78; 83; 93]. Considering that hard rocks are the primary targets of the EGS, we simplify our model by discarding the poroelastic and thermoelastic impacts for the rock matrix in Papers B, C and D. However, the 'effective stress' concept is applied for the determination of shear failure of fractures. The details about the fracture failure are provided in the next chapter.

3. Constitutive relations for deformation of pre-existing fractures

As presented in the previous chapter, the mechanical deformation of rock matrix can be approximated with the assumption of linear elasticity. However, the pre-existing fractures have distinctive constitutive relations for deformation which are mainly formulated with empirical approaches.

Depending on the stress state and mechanical properties, a fractured rock can exhibit three types of fracture deformation: shear deformation, irreversible normal deformation following the shear deformation, and reversible normal deformation. The fracture deformations, which alter the stress state of rock, are linked to permeability changes and induced seismicity. Thus, we start with the presentation of all these three types of deformations, and discuss their effect on permeability evolution and seismicity, beginning with the shear failure criterion. The shear failure criterion and resulting deformation are essential components of constitutive relations due to their primary effect on fracture permeability. Although there are other methods for determination of shear failure [59], we present the most well-known and perhaps also the most widely used criterion, which is Mohr-Coulomb. Also, several friction models to estimate frictional strength have been proposed for rock masses over the years. We also provide a small introduction to the most common friction models for rock surfaces.

Due to the different governing equations for fractures and rock matrix, we present the coupled problem of the deformation of fractured rock matrix at the end. This problem is solved in Paper A and coupled with fluid flow in Papers B, C, and D for hydraulic stimulation modeling.

3.1 The stress regimes and failure of fractured rocks

The stress field of the rock mass in the subsurface is created by a certain set of loads, for example, the weight of earth and the stresses created by the plate motions. For a stress field, $\boldsymbol{\sigma}$, which is described in terms of principal stresses, σ_1, σ_2, σ_3, the most common conditions of stress state in EGS in Europe are given as strike-slip $\sigma_1 > \sigma_2 > \sigma_3$ or normal faulting $\sigma_2 > \sigma_1 > \sigma_3$ [43], where σ_1 is the maximum horizontal stress, σ_2 is the vertical stress, and σ_3 is the minimum horizontal stress.

The stress field, $\boldsymbol{\sigma}$, provides traction vectors, $\boldsymbol{T}$, on fracture surfaces, which can be calculated using equation (2.6). The traction vectors, $\boldsymbol{T}$, have normal and shear components whose magnitudes are denoted as $T_{\boldsymbol{n}}$ and $T_{\boldsymbol{\tau}}$, respectively. Following the classical theory of friction, if the applied shear force exceeds the frictional strength of fracture faces, irreversible failure occurs in the direction of shear traction. Mohr-Coulomb theory defines the shear failure criterion by

$$T_{\tau} \geq S_0 + \mu_s T_{n,eff}, \tag{3.1}$$

where S_0 is the strength of the rock in absence of any normal stresses, $T_{n,eff}$ is the effective stress and μ_s is the static friction coefficient. μ_s ranges between 0.6 and 1.0 for almost all rock types, and the cohesive strength of the sliding surface, S_0, can be considered as negligible under typical crustal conditions [40]. Here, we exploit Terzaghi's effective stress definition:

$$T_{n,eff} = (T_n - p). \tag{3.2}$$

The shear resistance of the different fracture planes, which have different orientations, can be visualized by Mohr circle with failure curve, which is given in Figure 3.1. Moreover, the role of pressure can be easily shown in the same figure. Notably, this widely used failure criterion is constructed only by the maximum and minimum principal stresses; thus, it represents a simplification of actual rock behavior. However, it is considered to be extremely useful for understanding the effects of the stress state on rock failure [57].

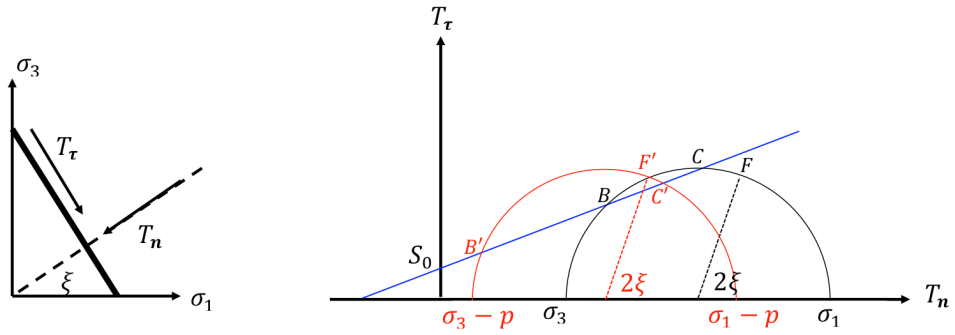

Figure 3.1: (Left) Fracture plane with outward normal vector oriented at angle ξ to the direction of maximum principal stress. (Right) Mohr circles with a failure curve. The black Mohr circle shows the initial (unpressurized) state and the red Mohr circle shows the pressurized state. The failure curve is shown by the blue line. For initial state, the normal and shear tractions along the fracture plane are represented by the point F. Shear slip will occur if the point F lies within arc BC of the Mohr circle. Due to the pressure, the failure arc becomes $B'C'$ and the stress location of fracture plane F' lies within arc $B'C'$ in this situation [57].

3.2 Friction models for fracture surfaces

The shear resistance of the pre-existing fractures can be determined with a static friction coefficient, μ_s, according to the Mohr-Coulomb theory. In addition, when the frictional resistance controls the fracture deformation, a dynamic friction coefficient, μ_d, should be defined. There are four common friction models for rock surfaces which all are motivated by experiments [33]. The common models can be listed:

static/dynamic friction model, slip-weakening model, time-weakening model, and rate- and state- dependent friction model.

The static/dynamic friction model

Two distinct friction values determine the friction coefficient of the fracture surfaces: the static friction coefficient, μ_s, and the dynamic friction coefficient, μ_d. If the shear stress of a fracture exceeds the Mohr-Coulomb failure criterion determined by μ_s, then its corresponding coefficient of friction is instantaneously lowered to a new dynamic value, μ_d. The $\mu_d > \mu_s$ relation is named as velocity-weakening model, where the shear strength of the fractures decrease with increased slip velocity. This model fits the failure behavior of fracture surfaces that are exposed to a sudden increase in slip velocity, in a very simplistic manner [37]. The static/dynamic friction model is denoted as an 'inherently discrete' method because the strength of the failing elements drops discontinuously with the slip [18; 95]. Although the model lacks convergence properties, it is reported to provide qualitatively acceptable results [77].

In all of our papers, we applied the static/dynamic friction model to calculate friction resistance prior to and after the shear slip.

The slip-weakening friction model

The friction of the fracture surfaces decreases from a static value, μ_s, to a dynamic value, μ_d, as slip progresses over a critical distance, d_c [7; 10].

The time-weakening friction model

The time-weakening friction model is analogous to the slip-weakening friction model. The only difference is that this model requires a critical time, t_c, for friction to decrease from a static value to a dynamic value [9].

The rate- and state- friction model

The Dieterich-Ruina rate and state friction model defines the friction by

$$\mu = \mu_0 + a \ln \frac{V}{V_0} + b \ln \left(\frac{V_0 \gamma}{d_c} \right), \tag{3.3}$$

where μ_0 is a friction coefficient measured at velocity V_0, V is the slip velocity, a and b are material coefficients and γ is a state variable [36; 37; 38]. The state variable, γ, which represents the irreversible mechanical deformations that occur during the sliding, is commonly defined as

$$\frac{d\gamma}{dt} = 1 - \frac{V_0 \gamma}{d_c} \tag{3.4}$$

[36; 37; 98]. Unlike the previously introduced friction models, the Dieterich-Ruina rate and state friction model can capture healing of friction after a high-velocity slip. With the help of coefficients a and b, both velocity-weakening and velocity-

strengthening mechanisms can be modeled. This may be essential for earthquake modeling where both seismic and aseismic slip should be captured [103]. This model does not suffer from convergence issues, on the other hand, incorporating this equation to modeling studies is significantly more computationally demanding than the previously introduced friction models due to the highly nonlinear terms [78].

3.3 Nonlinear fracture deformation

Laboratory investigations of various natural rock fracture samples have shown that the rough surfaces of the fractures deform with any alteration in the stress state of fractures [13; 14; 15; 16; 47]. In the context of shear stimulation, the main reason for stress alteration is the fluid injection. The injection changes the state of fluid pressure inside the fractures, which may lead to different types of fracture displacements according to the stress state and fracture characteristics. Here, we introduce three types of fracture displacements pertaining to shear stimulation: shear deformation, shear dilation, and normal deformation.

3.3.1 The shear displacement

The Mohr-Coulomb failure criterion states that the fracture surfaces displace in shear direction when the applied shear traction is greater than the shear resistance. Keeping in mind the static/dynamic friction model, the fracture surfaces have higher frictional strength prior to displacement and show a reduced level of frictional resistance after the displacement is initiated. The difference between static and dynamic strength causes a stress drop which is assumed to be the net force available to power a shear displacement once the failure has commenced [100]. The available net force driving the shear displacement is called ‘excess shear stress’ and defined as a difference between shear stress prior to slip and dynamic strength of the fracture faces [82; 93; 100]:

$$T_e = T_{\boldsymbol{\tau}} - \mu_d T_{\boldsymbol{n},eff}, \tag{3.5}$$

where T_e denotes the excess shear stress. The corresponding shear displacement following the stress drop can be approximated by exploiting the linear elastic theory:

$$\Delta d_s = \frac{T_e}{K_s'}, \tag{3.6}$$

where Δd_s is the shear displacement and K_s' is the fracture shear stiffness per area. K_s' is taken as a constant value for simplicity in Papers B, C and D; however, it has also been defined as a function of slip area in the related literature [90]. We use the excess shear stress concept in Papers B, C, and D to approximate the induced shear displacements. A more advanced model, in which the shear displacements are calculated by equating the shear stress to the dynamic frictional resistance, can also be used [77; 88].

3.3.2 The shear dilation

The shear displacement changes the surface characteristics of the fracture irreversibly owing to the asperity movement between fracture surfaces. The asperities slide over each other and lead to an increase in aperture, which is called shear dilation [15]. Dilation occurs in the normal direction with respect to the fracture surfaces and can be modeled by the following empirical relation [113]:

$$\Delta E_{n,irrev} = \Delta d_s \ tan\, \varphi_{dil}, \tag{3.7}$$

where φ_{dil} is the dilation angle that is measured experimentally, and suggested as a function of stress conditions [113]. The shear displacement and the dilation are presented in Figure 1.1.

3.3.3 The reversible normal deformation

In the laboratory experiments conducted by Goodman [47], the fracture closure (the change of the average aperture of the fracture) was measured as a function of normal stress, and a nonlinear relation was obtained between increasing normal stress and the closure of fractures. Goodman [47]'s experiments showed that fractures become more difficult to compress as the applied normal stress increases and that there is a maximum closure value. The laboratory investigations conducted by Bandis *et al.* [14] also showed that there is a non-linear and reversible normal-stress and normal-deformation relationship for fractures. This nonlinear relationship is described by Bandis *et al.* [14] as

$$\Delta E_{n,rev} = \frac{T_{\boldsymbol{n},eff}}{K_n' + \frac{T_{\boldsymbol{n},eff}}{\Delta E_{max}}}, \tag{3.8}$$

where $\Delta E_{n,rev}$ is the reversible normal deformation, ΔE_{max} is the maximum possible closure, and K_n' is given by

$$K_n' = \frac{\partial T_{\boldsymbol{n},eff}}{\partial \Delta E_{n,rev}} = \frac{K_{ni}'}{\left(1 - \frac{\Delta E_{n,rev}}{\Delta E_{max}}\right)^2}, \tag{3.9}$$

where K_{ni}' is the initial normal stiffness per area. For simplicity, the stiffness coefficient is assumed to be constant and equal to the initial stiffness in Papers B, C, and D.

Equation (3.8) gives the reversible deformation that occurs during the alteration of normal stress affecting the fractures. Notably, focusing on this relation, a detailed analysis of the reversible normal deformation and its contribution to the induced seismicity in hydraulic stimulations is discussed in Paper D.

The nonlinear normal deformation relation (equation (3.8)) with its counterpart in shear direction is named as the Barton-Bandis joint deformation model [15]. In addition to the Barton-Bandis joint deformation model, Willis-Richards model [113] is also commonly used in the literature [52; 65; 77; 93]. In this model, $\Delta E_{n,rev}$ is given by

$$\Delta E_{n,rev} = E_0 \left(1 - \frac{1}{1 + \frac{9T_{\boldsymbol{n},eff}}{T_{\boldsymbol{n},ref}}} \right). \tag{3.10}$$

Here, $T_{\boldsymbol{n},ref}$ is defined as the stress required to obtain 90 % closure of the aperture and E_0 is the aperture measured under zero stress conditions. The main differences between the Barton-Bandis joint deformation model and the Willis-Richards model are: the Willis-Richards model assumes the maximum possible closure is equal to the aperture measured under zero stress conditions and the stiffness coefficient is assumed to be constant and equal to the initial stiffness.

3.4 Fracture aperture and permeability evolution

The permeability of the fractures is determined by the mechanical apertures (void space between fracture faces). The empirical studies [14; 47] indicated that, first, the mechanical apertures between fracture surfaces can be measured under zero stress conditions, then, the deformation in the normal direction can be superposed to predict the final mechanical apertures which yield

$$E = E_0 - \Delta E_{n,rev} + \Delta E_{n,irrev}, \tag{3.11}$$

where E is the resulting mechanical aperture and E_0 is the mechanical aperture measured under zero stress conditions. $\Delta E_{n,rev}$ and $\Delta E_{n,irrev}$ are calculated according to the given relations in Section 3.3.

The permeability of fractures, K_f, is calculated by the cubic law (equation (2.3)). The cubic law assumes the fracture surfaces to be smooth parallel plates. However, the mechanical aperture of real fractures varies in space and is affected by several parameters such as wall friction and tortuosity [29]. Thus, another type of aperture, hydraulic aperture, is defined between fractured surfaces. Many researchers have conducted studies regarding to the relationship between mechanical and hydraulic aperture [15; 27; 94; 114]. One can use the joint roughness coefficient (JRC) to differentiate between aperture types [16], and the hydraulic aperture, e, can be calculated by considering the following relation suggested by Barton *et al.* [15]

$$e = \frac{E^2}{JRC^{2.5}}. \tag{3.12}$$

The JRC ranges between 0 and 20 and can be measured experimentally or by comparison with existing JRC values given by Barton and Choubey [16]. A large JRC indicates that the fracture surfaces are rough so that the shear movement between fracture surfaces is difficult. Note that the units in equation (3.12) are in μm and the equation is valid only for $E \geq e$.

3.5 Seismicity relations

The strength of the seismicity due the induced shear displacements is evaluated by calculating the seismic moment, M_0, and the moment magnitude, M_w, as

$$\begin{aligned} M_0 &= \int_A G \Delta d_s \, dA \\ M_w &= \frac{2}{3} \log M_0 - 6.07 \end{aligned}, \tag{3.13}$$

where G is the shear modulus and A is the slip area. In Papers C and D, the strength of the induced seismicity is analyzed by seismic moment calculations in each time step.

3.6 Coupling of deformation of fractures and rock matrix

Our particular interest is a stressed rock that includes pre-existing fractures. The fractures, which are denoted as Γ, are considered as two-sided co-dimension one inclusions in 2D or 3D domain, Ω. The fracture surfaces, which are considered as line pairs for 2D domains and face pairs for 3D domains, can displace relative to one another according to the fracture deformation equations presented in Section 3.3. Following the common notation in the related literature [2; 8; 32], we denote the two sides of the fracture inclusion by subscripts + and –, and we define the displacements on the positive and negative sides as $\boldsymbol{u}_+$ and $\boldsymbol{u}_-$, respectively. The illustration of the considered fractured formation is given in Figure 3.2.

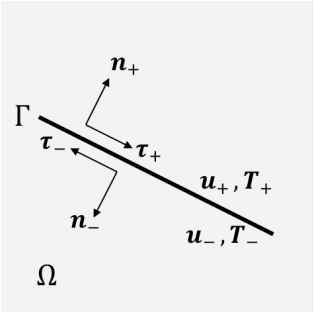

Figure 3.2: Modeling of a fracture retrieved from Paper A. Fractures are modeled as two-sided co-dimension one inclusions in the domain.

For a fracture plane that has a unit normal vector, the traction vector on the fracture can be found by using equation (2.6). Further, the relation between tractions on the fracture surfaces can be written as

$$\boldsymbol{T}_+ = -\boldsymbol{T}_-, \tag{3.14}$$

because of the equilibrium conditions where $\boldsymbol{T}_+$ and $\boldsymbol{T}_-$ are the tractions on the positive and negative side of the inclusion.

The fracture deformations are defined by a jump vector that is obtained by stress conditions (Section 3.3). The deformation response of the rock matrix to the fracture deformations can be obtained by solving the following set of equations,

$$\begin{aligned} \nabla \cdot \boldsymbol{\sigma} + \boldsymbol{f} &= 0 \text{ on } \Omega, \\ \boldsymbol{u} &= \boldsymbol{u}^D \text{ on } \partial\Omega^D, \\ \boldsymbol{T}(\boldsymbol{n}) &= \boldsymbol{T}^N \text{ on } \partial\Omega^N, \end{aligned} \tag{3.15a}$$

with the following internal boundary conditions:

$$\begin{aligned} \boldsymbol{T}_+ &= -\boldsymbol{T}_- \text{ on } \Gamma, \\ \boldsymbol{u}_+ - \boldsymbol{u}_- &= \Delta\boldsymbol{u}_f \text{ on } \Gamma \text{ where } \Delta\boldsymbol{u}_f = \boldsymbol{n}_+(\Delta E_{n,rev} + \Delta E_{n,irrev}) + \boldsymbol{\tau}_+ \Delta d_s, \end{aligned} \tag{3.15b}$$

where $\boldsymbol{T}(\boldsymbol{n})$ are the forces on the surfaces of Ω, identified by the outward normal vector $\boldsymbol{n}$, and $\boldsymbol{u}$ is the unknown displacement field. The two superscripts, *D* and *N,* denote Dirichlet and Neumann boundary conditions, respectively. The relative motion between the positive and negative surfaces, $(\boldsymbol{u}_+ - \boldsymbol{u}_-)$, are defined by a vector $\Delta\boldsymbol{u}_f$ in which $\boldsymbol{n}_+$ denotes the unit vector defining the normal direction of the positive side of the fracture and $\boldsymbol{\tau}_+$ denotes the unit vector defining the direction of the shear displacement (which points in the direction of maximum shear force) at positive side of the fracture. The positive face is considered as the reference to indicate the directions here, but the jump between the fracture faces can also be defined according to the negative fracture face. This problem is solved and analyzed for single- and multi-fractured 2D and 3D domains in Paper A. Moreover, the synthetic reservoirs considered in Papers B, C and D are exposed to displacement jumps; thus, the problem is solved for multiple-fractured 3D domains in these papers.

4. Numerical methods

The mathematical equations for the governing processes of shear stimulation are introduced in the previous chapter. Proper discretization methods and computational grids are required for the solution of the considered equations. Since the computational grid is profoundly connected to the numerical discretization, we introduce several grid types according to the used methods in the papers attached in Part II. For the numerical methods, we start with the finite volume methods (FVMs) for flow and mechanics discretization. The chapter continues with brief presentations of two common elasticity discretizations for fractured media: the finite element method (FEM) and the displacement discontinuity method (DDM). Further, upwind discretization is introduced for the advective term, $\mathcal{H}^{adv}$, in equation (2.10), and temporal discretization is provided for the time dependent terms in the conservation of mass (equation (2.1)) and conservation of energy equations (equation (2.10)). The chapter closes with the numerical coupling strategy that is applied for the modeling of shear stimulation.

4.1 Fractures in the grid

An example domain, which consists of fractures and rock matrix, is shown in Figure 4.1a. Depending on the computational method, the discretization can be conducted in various forms. Here, we present fracture implementation to the grids for the FVMs, FEM, and DDM used during the course of this thesis.

The discretizations for FVMs that are used here require dividing the computational domain into control volumes, Ω_i, conforming to the fractures as shown in Figure 4.1b. The primary variables are defined at centroids of the control volumes. The fracture discretization is customized according to the considered problem. For example, fluid flow occurs both inside of the fracture and the rock matrix; thus, the solution approximations of the fluid flow equations require discretizations in the fractures as well as in the rock matrix. In this case, the fracture discretization can be done by using a hybrid approach where the fractures are considered as lower dimensional objects [61; 101]. The hybrid approach converts the fractures into hybrid cells by assuming that the fracture is centered at the face and assigning an aperture to it. Then, the primary variable inside the fracture is associated with the hybrid cell centers. The volume of the hybrid cells is defined as the fracture volume, which is calculated by multiplying the area of the neighboring face by the aperture. An example grid for flow discretization with FVM is shown in Figure 4.1c. As for the FVM for flow discretization, the discretization for mechanics problem is done by considering the fractures as two-sided co-dimension one inclusions in the interior of the domain. Unlike the fluid flow problem, the inside of the fractures is not part of the solution, the fracture faces are the internal boundary conditions of the mechanical deformation problem. Thus, the computational grid, which is shown in Figure 4.1b, is

modified such that the edges of the grid corresponding to the fractures are duplicated. The vertices (edges in 3D) of the fracture edges are also duplicated. The vertices, which correspond to tips of the fractures interior to the domain, link the two faces on each side of the fractures. The primary variable for fracture faces is defined at the face centers. The resulting grid is presented in Figure 4.1d. Details of this approach are provided in Paper B.

The FEM also divides the computational domain into cells, Ω_i, and the grid structure for the rock matrix is again created such that the faces of the cells conform to the fracture faces. The main difference between FVM and FEM grid is the location of the primary variable, as FEM defines the primary variable at the vertices. Similar to the FVM developed for the mechanical deformation problem, FEM defines the fracture surfaces as parts of the solutions. An example FEM grid is shown in Figure 4.1e.

DDM requires a very distinctive grid compared to the previously introduced discretization schemes. DDM defines the unknowns only on the internal boundary of the problems [72]. Thus, only the fractures are divided into several segments. The rock matrix is not discretized in this method. An example grid for DDM is shown in Figure 4.1f.

For all the discretization techniques, the grid structures are created with the help of MATLAB Reservoir Simulation Toolbox (MRST) [70; 71]. MRST is an open-source reservoir simulator, which offers a wide range of data structures and computational methods. We also exploit Gmsh [44], especially for 3D discretizations.

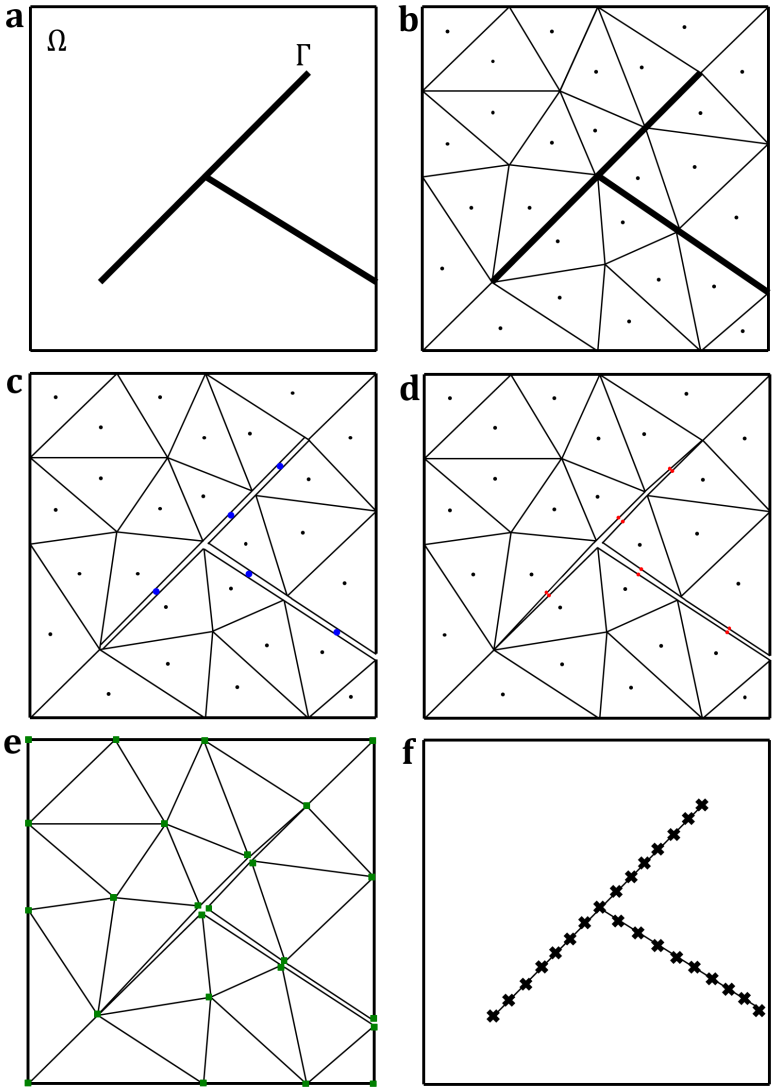

Figure 4.1: The grid structure of various discretization methods. (a) An example fractured domain. (b) Conforming finite volume mesh without considering the discretization of fractures. The locations for unknowns are shown with black dots. (c) Hybrid cells are created to represent fractures for flow discretizations with FVM. The unknown locations for hybrid cells are shown with blue dots. (d) The fracture faces are treated as internal boundaries for mechanical deformation discretizations with FVM. The gap between fracture faces is created for illustration purposes. In practice, the fracture faces do not preserve offset in the grid structure. The locations for unknowns at the fracture faces are shown with red dots. (e) The FEM grid in which the unknown locations are shown with green squares. (f) The fracture discretization for DDM where the locations for unknowns are shown with crosses.

4.2 Flux discretization for fractured rock

Two-point flux approximation (TPFA) [61], is a finite volume scheme, that can be used for the discretization of the diffusion terms in both conservation of mass (equation (2.1)) and conservation of energy equation (equation (2.10)). We start with a general steady-state conservation equation:

$$\nabla \cdot \boldsymbol{F} = \beta, \tag{4.1}$$

where β is a source/sink term, $\boldsymbol{F} = -\boldsymbol{\psi}\nabla\zeta$ for a quantity of ζ to be conserved and $\boldsymbol{\psi}$ is the conductivities i.e., permeability for mass conservation equation, and effective thermal conductivity for heat transfer equation. The above equation is integrated over the control volume Ω_i and the divergence theorem is applied for the flux term yields

$$\int_{\partial\Omega_i} \boldsymbol{n} \cdot \boldsymbol{F}\, dS = \int_{\Omega_i} \beta\, dV, \tag{4.2}$$

where $\boldsymbol{n}$ is the outward unit normal vector on boundary of cell volume, $\partial\Omega_i$. Denoting the quantity to be conserved by ζ, the flux across each face of s is F_s, is expressed in terms of ζ in the nearby cells, n_c,

$$F_s = -\int_S \boldsymbol{n} \cdot \boldsymbol{\psi}\nabla\zeta\, dS \approx \sum_{k=1}^{n_c} \gamma_k \zeta_k\,, \tag{4.3}$$

where γ_k is known as the face transmissibility. In the TPFA, the flux between two neighboring control volumes Ω_i and Ω_j is approximated as

$$Q_{ij} \approx \gamma_{ij}(\zeta_j - \zeta_i), \tag{4.4}$$

where ζ_i and ζ_j are the unknowns defined at the centers of cell i and cell j. The transmissibilities, γ_{ij}, corresponding to the face, $\mathcal{F}_{i,j}$, between the two cells, depend only on adjacent cells of the face, and are given by

$$\gamma_{ij} = \frac{\alpha_{i,\mathcal{F}_{i,j}}\, \alpha_{j,\mathcal{F}_{i,j}}}{\alpha_{i,\mathcal{F}_{i,j}} + \alpha_{j,\mathcal{F}_{i,j}}}, \tag{4.5}$$

where $\alpha_{i,\mathcal{F}_{i,j}}$ can be calculated as

$$\alpha_{i,\mathcal{F}_{i,j}} = \frac{A_{\mathcal{F}_{i,j}}\, \boldsymbol{n}_{\mathcal{F}_{i,j}} \cdot \boldsymbol{\psi}_i}{\boldsymbol{d}_{\mathcal{F}_{i,j}} \cdot \boldsymbol{d}_{\mathcal{F}_{i,j}}}\, \boldsymbol{d}_{\mathcal{F}_{i,j}}\,. \tag{4.6}$$

Here, $A_{\mathcal{F}_{i,j}}$ is the area of the face, $\boldsymbol{n}_{\mathcal{F}_{i,j}}$ is the unit normal vector pointing outward from cell i, $\boldsymbol{\psi}_i$ is the conductivity of cell i and $\boldsymbol{d}_{\mathcal{F}_{i,j}}$ is the distance vector from the centroid of cell i to the face centroid. Transmissibilities are calculated between

neighbor rock matrix cells, between neighbor hybrid cells, and between neighbor rock matrix and hybrid cells.

Notably, to be consistent, TPFA requires using K-orthogonal grids, i.e., anisotropy has to align with the grid. K-orthogonal requirement limits the usability of the TPFA for anisotropic permeability fields. A remedy can be using multipoint flux approximation (MPFA) where the discretization is done by using multiple points instead of two [3]. MPFA is reported to be robust and applicable for general grids; however, the method has disadvantages regarding computational expense [3; 101].

In Papers B, C, and D, isotropic permeability/thermal conductivity is assumed for the rock; thus, we have chosen to use TPFA, which is applied for the discretization of all diffusive terms with the help of MRST [70; 71].

4.3 Elasticity discretization for fractured rock

This section includes the introduction of the method developed in Paper A and the most common elasticity discretization methods for domains that expose displacement jumps. The discretizations are introduced by focusing on the problem described by equation (3.15), as the displacement jumps induced by stimulation is our interest.

4.3.1 Multi-point stress approximations

The multipoint stress approximation (MPSA) is a recent method to model mechanical deformation in porous media [62; 84; 85; 86]. It is proposed as a compatible counterpart to finite-volume flow calculations, with the key advantage that it uses the same data structure with cell-centered flow discretizations. MPSA is explicitly formulated to handle discontinuities and heterogeneous material, which is the target domain of this thesis. Specifically, in the MPSA discretization, the traction forces have explicit expressions at the grid faces. This property is particularly attractive for us because it provides a natural fracture (discontinuity) implementation to the discretization.

The static momentum balance equation ignoring the inertia forces can be written for each cell in integral form

$$-\int_{\Omega_i} \boldsymbol{f} dV = \int_{\partial\Omega_i} \boldsymbol{T}(\boldsymbol{n}) dA, \tag{4.7}$$

where $\boldsymbol{T}(\boldsymbol{n})$ are the surface traction vectors on the boundary of some domain with outward facing normal vector $\boldsymbol{n}$. The discrete form of equation (4.7) can be written as

$$-\boldsymbol{f}_i = \frac{1}{|\Omega_i|} \sum_j \boldsymbol{T}_{i,j}, \tag{4.8}$$

where $\boldsymbol{T}_{i,j}$ is the stress over face $\mathcal{F}_{i,j}$ which is between cells i and j, and $-\boldsymbol{f}_i$ is the volume-averaged force over cell Ω_i. The discrete stress, $\boldsymbol{T}_{i,j}$, is defined as a linear function of displacements:

$$\boldsymbol{T}_{i,j} = \sum_{\mathrm{k}} \tilde{t}_{i,j,k} \boldsymbol{u}_k, \tag{4.9}$$

where $\tilde{t}_{i,j,k}$ are referred as stress weight tensors and $\boldsymbol{u}_k$ are the displacements located at cell centers. The MPSA discretization divides the cells into one sub-cell per vertex, and all sub-cells associated with a vertex, l, form an interaction region, see Figure 4.2. The gradients, which are denoted as $\boldsymbol{G}_{i,l}$, are defined in each sub-cell, $\tilde{\Omega}_{i,l}$. Each component of the displacement is approximated by a multi-linear function of the spatial coordinates, such that

$$\boldsymbol{u} \approx \boldsymbol{u}_i + \boldsymbol{G}_{i,l} \cdot (\boldsymbol{x} - \boldsymbol{x}_i), \tag{4.10}$$

where $\boldsymbol{u}_i$ is the cell-average displacement, $\boldsymbol{x}_i$ is the cell-center, $\boldsymbol{x}$ is a point within the sub-cell $\tilde{\Omega}_{i,l}$.

The stress weight tensors, $\tilde{t}_{i,j,k}$, are calculated by imposing continuity of surface stresses and displacements over a sub-face by local calculations in each interaction region. After the calculation of stress-weight tensors, the final discrete form of the force-balance equations is obtained by

$$-\boldsymbol{f}_i = \frac{1}{|\Omega_i|} \sum_j \sum_k \tilde{t}_{i,j,k} \boldsymbol{u}_k \,. \tag{4.11}$$

So far, the created force-balance system does not include the fractures. In Paper A, we incorporate constitutive models for fracture deformation into equation (4.11) via internal boundary conditions. We simply define the displacements on each side of the fracture by equation (4.10)

$$\begin{aligned} \boldsymbol{u}_{i,s,+} &= \boldsymbol{u}_i + \boldsymbol{G}_{i,l}\left(\tilde{\boldsymbol{x}}_{i,m,l} - \boldsymbol{x}_i\right), \\ \boldsymbol{u}_{i,s,-} &= \boldsymbol{u}_s + \boldsymbol{G}_{s,l}\left(\tilde{\boldsymbol{x}}_{s,m,l} - \boldsymbol{x}_s\right), \end{aligned} \tag{4.12}$$

where $\tilde{\boldsymbol{x}}_{i,m,l}$ and $\tilde{\boldsymbol{x}}_{s,m,l}$ are the split continuity points on sub-face $\tilde{\mathcal{F}}_{i,m,l}$ and $\tilde{\mathcal{F}}_{s,m,l}$. The coupled fracture-matrix deformation problem, which is introduced in Section 3.6, is solved in Paper A (see Paper A for details). In Papers B, C, and D, the developed method in Paper A (MPSA with fractures) is applied to obtain stress alterations in the fractured rock caused by the fracture deformations.

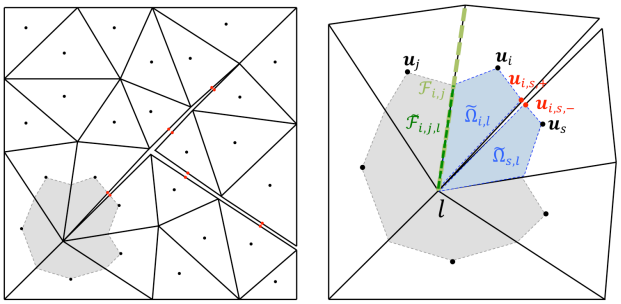

Figure 4.2: MPSA grid details (retrieved from Paper A). (Left) MPSA grid with fractures. (Right) An example interaction region. The fracture faces are located between cells i and s. While the unknowns $\boldsymbol{u}_i$ and $\boldsymbol{u}_s$ represent the displacements in the cell centers of i and s, the unknowns $\boldsymbol{u}_{i,s,+}$ and $\boldsymbol{u}_{i,s,-}$ represent the discrete displacements on the fracture surfaces. For clarity, the colors of light green, dark green, and blue are associated with the faces, sub-faces, and sub-cells, respectively.

4.3.2 Alternative discretization methods

As we have only applied MPSA for the deformation of fractured domains and used the alternative techniques just for comparison in Paper A, the alternative methods are introduced briefly. Detailed presentations are provided in the suggested references.

Finite element method (FEM)

FEM has been one of the most popular numerical methods for a wide range of disciplines. The popularity is due to its well-established mathematical background, flexibility in gridding, and handling of material heterogeneity, complex boundary conditions, and dynamic problems, etc. [2; 17; 59; 64; 66; 115].

FEM makes use of test functions, $\boldsymbol{\omega}$, to create weak form of the considered equations:

$$\int_{\Omega} \boldsymbol{\omega} \cdot (\boldsymbol{\nabla} \cdot \boldsymbol{\sigma} + \boldsymbol{f}) d\,V = 0. \tag{4.13}$$

The discretization of the weak form is obtained by defining a trial solution, $\boldsymbol{u}$ as linear combinations of a set of basis functions:

$$\boldsymbol{u} = \sum_{j=1}^{m} a_j N_j, \tag{4.14}$$

where a_j are nodal values of the trial solution and m the number of the basis functions, $\{N_j\}$. In standard Galerkin FEM, the basis functions have local support. Depending on the considered problem/method, basis functions can be chosen as linear or higher degree polynomials. The discrete form of equation (4.13) is obtained by substituting the trial solution (equations (4.14)) with the basis functions as

successive test functions into equation (4.13). Then, the discrete form with boundary conditions is reformulated as an nxn system of algebraic equations.

In case of domains with discontinuities, the tractions at the fracture surfaces and displacement jump between the fracture surfaces are also approximated with basis functions. The three commonly used methods for imposing the fracture deformation equations: the Lagrange multipliers method, the penalty method, and the augmented Lagrangian method [23]. An open source FEM software, Pylith [1; 2], which imposes the fracture tractions with Lagrange multipliers is used in Paper A to compare the convergence properties of MPSA with FEM for a case in which the domain includes a discontinuity.

Displacement Discontinuity Method (DDM)

DDM is an indirect boundary element method which is developed by Crouch and Starfield [32] and Shou and Crouch [104] to model the deformation of elastic media containing discontinuities. It has been a preferred method in the literature [4; 48] due to its relatively easy implementation and lower memory demands. DDM divides the fractures into N elemental segments with the displacement in each segment assumed to have a constant discontinuity. At any point, induced stresses can be found by summing the effects of all N elements using the fundamental analytical solutions. The linear system is structured in the form of

$$\Delta\boldsymbol{\sigma}_i = \sum_{j=1}^{N} \boldsymbol{B}_{ij} \Delta\boldsymbol{u}_{f_j}, \tag{4.15}$$

where $\Delta\boldsymbol{\sigma}_i$ is the induced stresses at element i, $\boldsymbol{B}_{ij}$ is the matrix of interaction coefficients, and $\Delta\boldsymbol{u}_{f_j}$ is the given displacement jump. The interaction coefficients are calculated according to fundamental analytical solutions [32].

DDM has developed as a 2D method and has been extended to 3D applications [67]. The main disadvantage of DDM is the difficulty of treatment of heterogeneous materials [59].

4.4 Upwind Discretization

An upwind discretization is applied for the advective term in the heat transfer equation, $\mathcal{H}^{adv}$, which is the energy that is transported by the flow. The amount of advective heat transfer over the face $\mathcal{F}_{i,j}$ between the two cells with index i and j is approximated by exploiting the flux direction:

$$\mathcal{H}^{adv}_{\mathcal{F}_{i,j}} \approx \boldsymbol{w}_{\mathcal{F}_{i,j}} \theta_{upwind,ij}, \tag{4.16}$$

where $\boldsymbol{w}_{\mathcal{F}_{i,j}}$ is the flux, and $\theta_{upwind,ij}$ is calculated as

$$\theta_{upwind,ij} = \begin{cases} \theta_i \; if \; \boldsymbol{w}_{\mathcal{F}_{i,j}} \cdot \boldsymbol{n}_{\mathcal{F}_{i,j}} \geq 0, \\ \theta_j \; if \; \boldsymbol{w}_{\mathcal{F}_{i,j}} \cdot \boldsymbol{n}_{\mathcal{F}_{i,j}} < 0. \end{cases} \tag{4.17}$$

While $\boldsymbol{w}_{\mathcal{F}_{i,j}} \cdot \boldsymbol{n}_{\mathcal{F}_{i,j}} > 0$ indicates that the flow direction is from cell i to j, and $\boldsymbol{w}_{\mathcal{F}_{i,j}} \cdot \boldsymbol{n}_{\mathcal{F}_{i,j}} < 0$ indicates that the flow occurs from cell j to i.

4.5 Temporal Discretization

The solution of the mass conservation equation and the heat transfer equations require time discretization. In Papers B, C, and D, we use implicit Euler method; thus, the presentation here is limited to this scheme.

For an unknown field of ζ, the general system of equations is in the form of

$$\frac{\partial \zeta}{\partial t} = S(\zeta) \tag{4.18}$$

where S is function obtained through the spatial discretization. The implicit Euler scheme approximates the unknown field for time step $\mathrm{t}+1$, ζ^{t+1}, by using S values evaluated at the time step $\mathrm{t}+1$:

$$\frac{\zeta^{t+1} - \zeta^{t}}{\delta t} = S(\zeta^{t+1}) \tag{4.19}$$

where ζ^t is the unknown field at the time step t and δt is the time step length.

4.6 Numerical coupling strategy

The shear stimulation modeling requires coupling three main processes: fluid flow, stress alteration, and fracture deformation. For example, the pressure term affects the fracture deformation in both reversibly and irreversibly. Fracture deformation changes the aperture and thus the permeability of the fractures, and the rock matrix responds to both irreversible and reversible fracture deformation, which creates a stress alteration both in the rock matrix and fracture surfaces. The stress state of the fractures also influences the mechanical apertures of the fractures.

The following relations can be given as a summary of interconnections:

$$\begin{aligned} E_m &= E_m(\boldsymbol{\sigma}, p), \\ p &= p(E_m), \\ \boldsymbol{\sigma} &= \boldsymbol{\sigma}(E_m). \end{aligned} \tag{4.20}$$

We have developed a two-stage sequential coupling approach in Papers B and C, which captures these interrelations. Paper B includes a premature version of the coupling strategy that is applied in Paper C. In Paper B, the two problems of flow and

mechanics are solved sequentially without iterations. First, the fluid flow problem is solved, and then the Mohr-Coulomb criterion is checked to obtain induced displacements. The induced displacements are given as internal boundary conditions to the conservation of momentum equations. The Mohr-Coulomb criterion is rechecked after the stress redistribution to capture possible additional shear displacements. This coupling strategy cannot capture the effect of the pressure to the elastic deformations of fractures; thus, the coupling strategy is improved in Paper C.

In Paper C, a two-stage procedure is developed and applied at each time step. We can summarize that the first stage pertains to the reversible fracture deformation and its effects to flow and mechanics, and the second stage is related to irreversible fracture deformation and its effects to flow and mechanics.

At the beginning of each time step, the first stage starts with solving the flow problem using the pressure distribution from the previous time-step. By using the obtained pressure field, iteration is started between reversible (elastic) fracture deformation, fluid flow and stress alteration of the rock matrix. This iteration between fluid flow, mechanical aperture and mechanical response of the matrix continues until convergence of mechanical aperture is obtained. It is observed that the convergence of mechanical aperture requires more iteration than pressure or displacement convergence. Thus, we choose convergence of mechanical aperture as stopping criteria for the iteration.

After the convergence of mechanical aperture, the second stage is performed to obtain the shear failure of the fractures and the corresponding stress alteration of the rock matrix. In this stage, the stress alteration in the system is assumed to be instantaneous relative to the fluid flow; therefore, the pressure distribution is held fixed. The Mohr-Coulomb criterion is applied for each fracture face to capture the shear failure. When a shear stress is higher than the frictional resistance of the fracture face, the shear displacements are initiated. The shear displacements create irreversible normal deformations (dilations) on the fracture surfaces. Then, these fracture deformations are defined as internal boundary conditions to the mechanics problem to obtain the stress alterations in the system. The stress alterations in the domain can increase and decrease the shear and normal stresses at some locations; thus, further failures can be initiated, which are also named as ‘slip avalanches’ [12]. Hence, following a shear failure, the mechanical state of the system is recalculated, and the Mohr-Coulomb criterion successively checked for all fractures. This continues until the system reaches an equilibrium state in which additional displacements are no longer induced and the next time step is executed. The solution summary for each time step is illustrated in Figure 4.3, which is retrieved from Paper C.

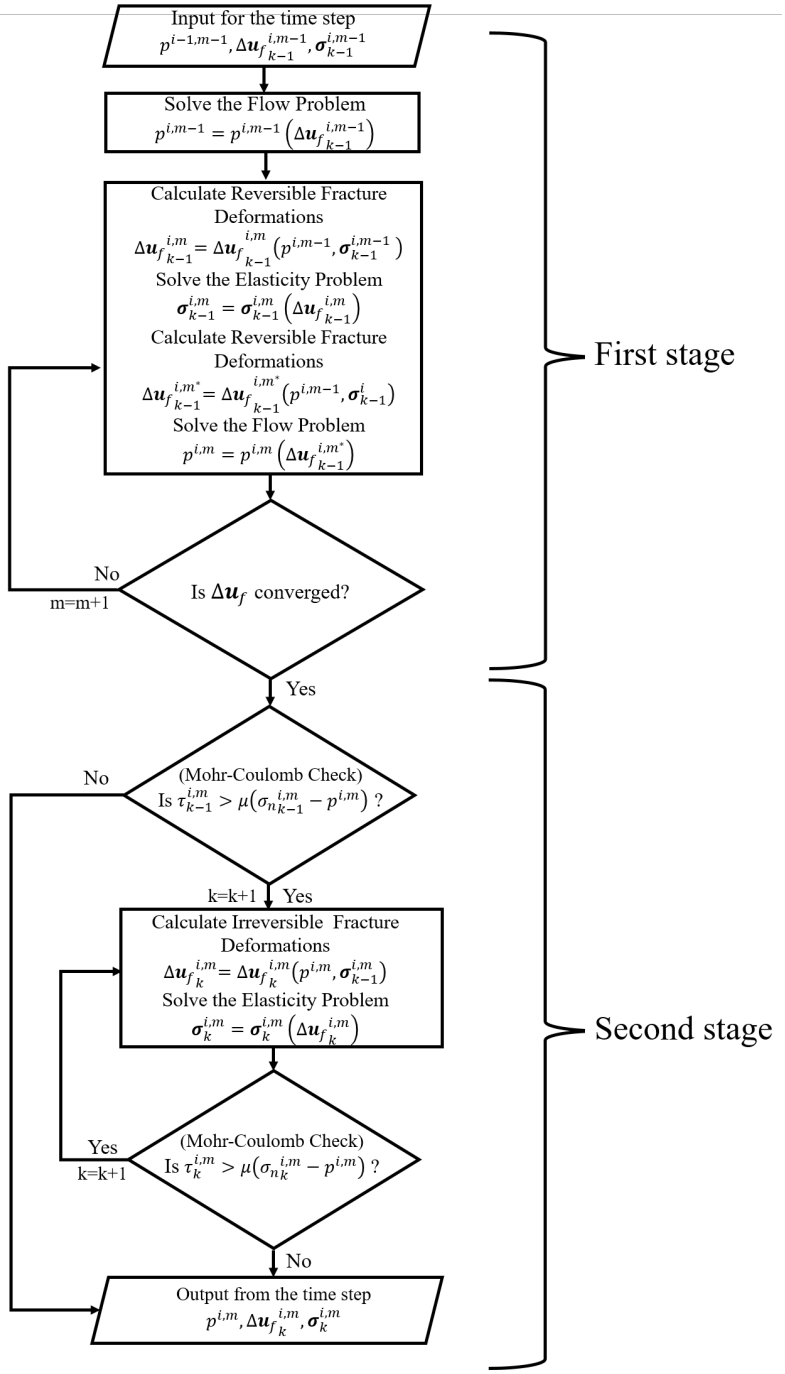

Figure 4.3: The two-stage solution procedures to model shear stimulation. The figure is retrieved from Paper C.

5. Main findings and outlook

Part I of the thesis is finalized with this chapter. Here, summaries of the main findings, which are presented in the papers attached in Part II, are provided. The chapter ends with an outlook.

5.1 Summary of papers

5.1.1 Summary of Paper A

An existing cell centered discretization method for linear elastic deformation is augmented to include deformation of discontinuities, i.e., fractures. The study is motivated by the fact that the subsurface formations preserve slit-like discontinuities, which have different governing equations than the rock, and they dominate the mechanical behavior. Thus, the proper modeling of rock mechanics requires efficient incorporation of fractures. Our method builds upon the recently developed multi-point stress approximations (MPSA) [62; 84; 85; 86], which are introduced as a counterpart of cell-centered fluid flow discretizations. Hence, the method aims to provide benefits especially for modeling studies that include hydromechanical coupling in fractured formations.

Simulations of several subsurface applications require mathematical modeling of coupled fluid flow and mechanical deformation in fractured formations. Modeling literature generally relies on different types of discretization schemes for the solutions of the flow and mechanics problem. Fluid flow is generally approximated by FVMs owing to their conservation properties. However, the mechanical deformation of discontinuous rock is approximated mainly using two approaches: boundary-element methods and FEM [4; 6]. The main contribution of the Paper A is to provide an opportunity to use the same data structure for the solution of flow and mechanics problems. Notably, the proposed method is not the first method that applies finite volume discretization in discontinuous media; recently, Deb and Jenny [34] have developed an FVM for fractured formations and successfully coupled it with the flow problem in 2D domains. The method presented in their study uses a structured grid for matrix discretization, and the discrete fractures are embedded in the domain. Our method carries the finite volume discretization one step further and applies it to the 3D domains with 2D complex fracture networks.

In Paper A, the subsurface rock is considered as a combination of explicitly represented pre-existing fractures and the rock matrix surrounding them. The pre-existing fractures are incorporated into the model as co-dimension one inclusions. The rock matrix is assumed to be a linearly deforming elastic material [57], and fractures are allowed to preserve various kinds of governing equations according to the application area. The two fracture surfaces are defined as internal boundary conditions to the linear elastic domain, and the governing relations for fractures are

defined as relations between the fracture faces. The existing literature generally targets only one or two types of fracture deformation [2; 32; 88], the method developed here contributes to the literature such that it can be tailored to incorporate various kinds of governing equations for fracture deformations. Three types of fracture deformation equations, which are commonly encountered in subsurface applications, are considered. The first type is the displacement jump controlled fracture deformations. The second type tackles the deformation behavior of fractured formations when stress conditions are applied to the fracture faces. The last problem is created to approximate the mechanical behavior of fractured rock when the displacements are controlled by friction between fracture surfaces.

The validation of the developed method is performed in three ways. First, the convergence properties of the presented method are discussed against analytical solutions, which are defined in single-fractured 2D domains. The comparisons with analytical solutions show that the method generally displays 1st order convergence for displacement, which is lower than in previous numerical studies of MPSA methods without fractures. The reduced convergence order is considered to be natural when the domain includes a discontinuity. Second, the convergence examination of the method is done in a 2D domain that includes a complex fracture network. The fracture network is created with 10 fractures with irregular orientations. The reference solution for this problem is obtained using a relatively fine grid. The convergence is observed to be higher than 1st order in this case. As a final examination, the method is compared with FEM [1] in a 3D domain that includes a single fracture in the middle. The convergence ratio is found to be slightly higher than 1 for FEM and slightly lower than 1 for MPSA, while the errors are of the same magnitude for both methods.

5.1.2 Summary of Papers B and C

In the Papers B and C, we present a new modeling framework for shear stimulations performed in low permeable geothermal reservoirs.

One of the main advantages of our method is the representation of the rock as a discrete fracture-matrix (DFM) system, which subdivides the domain into the explicitly represented fractures and the rock matrix [61]. Whereas the related literature either models the geothermal reservoir as a continuum or ignores the mass exchange between fractures and the rock matrix [26; 58; 77; 112], the study contributes to the literature by capturing discrete effects of each fracture while still considering the fluid leakage to the rock matrix.

In the DFM system, three governing mechanisms are coupled: (i) fluid flow in both fractures and rock matrix, (ii) nonlinear fracture deformation, and (iii) linear rock matrix deformation in the 3D domain. In the presented model, the fluid flow in the reservoir is obtained by solving conservation of mass equations with Darcy's law in both rock matrix and fractures. While permeability of the rock matrix is considered as a material specific constant number, the fracture permeabilities are associated with the gap between fracture surfaces, i.e., apertures, via the cubic law [57].

The change in the pressure field deforms the fractures in both normal and tangential direction with respect to the fracture plane. In the normal direction, the deformation of the fractures has elastic nature, which is modeled following the nonlinear Barton-Bandis joint deformation model [15; 47]. In the tangential direction, the deformation is captured by Mohr-Coulomb criterion with static/dynamic friction model. For any fracture element that violates the criterion, the resulting irreversible linear deformation (shear deformation) is calculated according to the relations suggested by Ryder [100], Napier and Malan [82] and Rahman *et al.* [93]. The static/dynamic friction model has a drawback of being discretization dependent. A remedy can be using advanced friction models, which are computationally very expensive [78]. Alternatively, better estimations of shear slip can be achieved with an improvement that is suggested to the numerical coupling procedure of the current method by Berge *et al.* [19].

Following the shear deformation, the fracture faces are exposed a somewhat wearing that leads to a dilation in the normal direction of the fracture [15; 113]. The dilation (a.k.a. shear dilation) increases the aperture between fracture surfaces, which enhances the permeability of fractures according to the cubic law. While the dilation alters the fluid flow characteristic of the entire reservoir, the fracture deformations cause deformation of the rock matrix and alter the stress state of the rock. The stress alteration is captured by conservation of momentum principle by assuming that the rock matrix acts as an elastic material that deforms linearly following fracture deformations. The coupling of rock matrix and fractures are provided via representing fractures as two-sided co-dimension one inclusions in the rock matrix.

Both of the conservation equations are approximated by using FVM with special treatment for the fractures. The discretization of mass conservation equations is conducted with a commonly applied cell centered method with converting fractures to hybrid cells in the grid [61]. Unlike the traditional methods in the literature for the solutions of conservation of momentum equations such as FEM and DDM, the method enjoys same data structure for two different differential equations (flow and mechanics) by using the method developed in Paper A.

The initial version of the model is introduced in Paper B. The method is applied to a 2D domain, which has several fractures with various orientations. In Paper B, we provide detailed visualizations of the induced shear displacements. Moreover, the effect of matrix permeability is emphasized via simulations that are conducted with different matrix permeability values.

Paper C presents an improved version of the Paper B in terms of both coupling strategy and the dimension of the method. Here, the improved version is verified by conducting three cases in a 3D synthetic reservoir which hosts 20 fractures. The first of the three cases emphasizes the effects of the complex structure of fracture network on the permeability enhancement and induced seismicity. In the second case, the significance of the mass exchange between fractures and rock matrix on the shear stimulation is examined. We show that the rock matrix permeability has significant effects on both permeability enhancement and induced seismicity; thus, ignoring rock

matrix permeability may lead to inaccurate estimations. Finally, we take the results of our model from the stimulation experiments and apply to a production scenario. The effect of shear stimulation on the temperature profile of the reservoir is demonstrated by comparing the results of the same production scenario with the stimulated and un-stimulated reservoirs.

5.1.3 Summary of Paper D

In this work, the developed model in Paper C is used to aid understanding the contributing mechanisms to postinjection seismicity that has been observed after the stimulation of several reservoirs [5; 39; 51].

The spatiotemporal distributions of induced seismicity in Basel and Paralana geothermal projects show that the locations of seismic events after the termination of injection are mainly at the outer rim of the previous seismic activity region [5; 51; 80]. We evaluate a novel hypothesis regarding causes of the postinjection seismicity in this region.

The laboratory experiments conducted by Bandis *et al.* [14] and Barton *et al.* [15] indicated that the fracture deformation has nonlinear elastic characteristics in the normal direction with the applied normal stress. If the fluid pressure is increased in the fractures, the aperture increases, and the opposite effect occurs when the pressure decreases. The hypothesis in this study is motivated due to the fact that the pressure decreases after the termination of injection in the close proximity to the injection well, which causes a reduction in apertures. Reduced aperture acts as a postinjection pressure support to advance the front of the elevated fluid pressure and cause seismic events and corresponding increases in apertures beyond the previously stimulated region.

The effect of the normal closure of fractures is qualified by examining two cases (Case 1 and Case 2) under two different scenarios; with and without the normal closure mechanism included after the termination of the injection. Case 1 demonstrates the normal closure effect in a single-fractured 3D domain in detail. The second case includes an analysis of a 3D domain that consists of 20 penny-shaped fractures. Both of the cases suggest that the normal closure of fractures should be considered a significant mechanism that leads to elevated postinjection seismicity.

There have been several attempts to investigate the governing mechanisms of the postinjection seismicity in the literature [12; 43; 65; 76; 77]. The contribution of this study is to identify and assess a mechanism that has been overlooked previously.

5.2 Outlook

An important goal for EGS is to identify optimum stimulation techniques for a geological structure in a safe setting. While shear stimulation with rate controlled fluid injection can be an optimum choice for a certain reservoir, a pressure controlled

cyclic injection technique can be preferable for others. The simulation method developed here can aid both decisions of the best technique for each geological setting and mitigation of elevated seismicity. Depending on the target application area, the method presented here can be used or extended. Thus, the further work related to the presented method can be both application-based and model-development-based.

The presented method can be applied in various geological settings. There are no known theoretical limitations of the method in terms of the considered fracture network or physical parameters. For example, the method can be applied to a more realistic fracture network generated by outcrop and borehole studies. The seismic recordings from boreholes can estimate the 3D structure of a reservoir as in Sausse *et al.* [102], and the recorded seismic response of the reservoir to stimulation experiments can be used for calibration of the methodology presented in this thesis. However, the computational intensity caused by the size of the considered problem should not be discarded.

In terms of model development, including the thermal effect can be considered as a priority. Depending on the rock structure of the target application area, the method could be extended to include thermoelasticity and poroelasticity. Moreover, two-phase or three-phase fluid flow can be added if one would like to benefit from the method for simulations requires modeling of different phases such as in CO_2 injections or water flooding.

The current method provides a qualitative analysis regarding induced seismicity due to the considered static/dynamic friction model. More accurate estimations can be achieved by implementing more advanced friction models such as rate- and state-friction model [36; 37; 38; 98]. Although the implementation of an advanced friction model also solves the convergence problem that the current model preserves, these models are reported to be computationally very expensive [78].

It should be noted that fracture deformation remains one of the major challenges due to its complex nature, which is defined by empirical correlations based on the experimental analysis. The fracture deformation in laboratory experiments is essentially different from the real reservoir conditions mainly because of the scale differences [99]. Further work can include characterizing the scale difference and representing it in the developed model. Also, the modeling of wing fractures, which may occur at the tip of fractures as a result of shear stimulations [79], remains future work.

On the other hand, a trade-off exists between the number of physical processes considered and the efficiency of the method due to the computational cost. The numerical methods are developed to provide a better understanding of the overall behavior and to assist solution of practical problems. Hence, the numerical models will always require simplifications and idealizations while still aiming at maintaining the necessary level of complexity according to the target problem.

References

[1] B.T. Aagaard, S. Kientz, M.G. Knepley, L. Strand, and C. Williams, PyLith user manual, version 2.1.0, Davis, CA, 2015.

[2] B.T. Aagaard, M.G. Knepley, and C.A. Williams, A domain decomposition approach to implementing fault slip in finite-element models of quasi-static and dynamic crustal deformation. Journal of Geophysical Research: Solid Earth 118 (2013) 3059-3079.

[3] I. Aavatsmark, An introduction to multipoint flux approximations for quadrilateral grids. Computational Geosciences 6 (2002) 405-432.

[4] J. Adachi, E. Siebrits, A. Peirce, and J. Desroches, Computer simulation of hydraulic fractures. International Journal of Rock Mechanics and Mining Sciences 44 (2007) 739-757.

[5] J. Albaric, V. Oye, N. Langet, M. Hasting, I. Lecomte, K. Iranpour, M. Messeiller, and P. Reid, Monitoring of induced seismicity during the first geothermal reservoir stimulation at Paralana, Australia. Geothermics 52 (2014) 120-131.

[6] T.L. Anderson, Fracture mechanics: fundamentals and applications, CRC press, 2005.

[7] D.J. Andrews, Dynamic plane-strain shear rupture with a slip-weakening friction law calculated by a boundary integral method. Bulletin of the Seismological Society of America 75 (1985) 1-21.

[8] D.J. Andrews, Test of two methods for faulting in finite-difference calculations. Bulletin of the Seismological Society of America 89 (1999) 931-937.

[9] D.J. Andrews, Rupture models with dynamically determined breakdown displacement. Bulletin of the Seismological Society of America 94 (2004) 769-775.

[10] D.J. Andrews, Rupture dynamics with energy loss outside the slip zone. Journal of Geophysical Research: Solid Earth 110 (2005).

[11] G.E. Association, 2016 Geothermal power: International market update. in: A. Rocco, (Ed.), http://www.geo-energy.org, Washington, D.C., 2016.

[12] S. Baisch, R. Vörös, E. Rothert, H. Stang, R. Jung, and R. Schellschmidt, A numerical model for fluid injection induced seismicity at Soultz-sous-Forêts. International Journal of Rock Mechanics and Mining Sciences 47 (2010) 405-413.

[13] S. Bandis, A. Lumsden, and N. Barton, Experimental studies of scale effects on the shear behaviour of rock joints. International Journal of Rock Mechanics and Mining Sciences & Geomechanics Abstracts 18 (1981) 1-21.

[14] S. Bandis, A. Lumsden, and N. Barton, Fundamentals of rock joint deformation. International Journal of Rock Mechanics and Mining Sciences & Geomechanics Abstracts 20 (1983) 249-268.

[15] N. Barton, S. Bandis, and K. Bakhtar, Strength, deformation and conductivity coupling of rock joints. International Journal of Rock Mechanics and Mining Sciences & Geomechanics Abstracts 22 (1985) 121-140.

[16] N. Barton, and V. Choubey, The shear strength of rock joints in theory and practice. Rock Mechanics 10 (1977) 1-54.

[17] K.-J. Bathe, Finite element procedures, Klaus-Jurgen Bathe, 2006.

[18] Y. Ben-Zion, and J.R. Rice, Earthquake failure sequences along a cellular fault zone in a three-dimensional elastic solid containing asperity and nonasperity regions. Journal of Geophysical Research: Solid Earth 98 (1993) 14109-14131.

[19] L.R. Berge, I. Berre, and E. Keilegavlen, Reactivation of Fractures in Subsurface Reservoirs - a Numerical Approach using a Static-Dynamic Friction Model, submitted to ENUMATH, Springer, Voss, 2017.

[20] R. Bertani, Geothermal power generation in the world 2010–2014 update report. Geothermics 60 (2016) 31-43.
[21] M.A. Biot, General theory of three-dimensional consolidation. Journal of Applied Physics 12 (1941) 155-164.
[22] J.J. Bommer, S. Oates, J.M. Cepeda, C. Lindholm, J. Bird, R. Torres, G. Marroquín, and J. Rivas, Control of hazard due to seismicity induced by a hot fractured rock geothermal project. Engineering Geology 83 (2006) 287-306.
[23] R.I. Borja, Plasticity, Springer, 2013.
[24] M. Bott, and N. Kusznir, The origin of tectonic stress in the lithosphere. Tectonophysics 105 (1984) 1-13.
[25] K. Breede, K. Dzebisashvili, X. Liu, and G. Falcone, A systematic review of enhanced (or engineered) geothermal systems: past, present and future. Geothermal Energy 1 (2013) 4.
[26] D. Bruel, Using the migration of the induced seismicity as a constraint for fractured hot dry rock reservoir modelling. International Journal of Rock Mechanics and Mining Sciences 44 (2007) 1106-1117.
[27] F. Cappa, Y. Guglielmi, P. Fénart, V. Merrien-Soukatchoff, and A. Thoraval, Hydromechanical interactions in a fractured carbonate reservoir inferred from hydraulic and mechanical measurements. International Journal of Rock Mechanics and Mining Sciences 42 (2005) 287-306.
[28] T.J. Centner, and L.K. O'Connell, Unfinished business in the regulation of shale gas production in the United States. Science of the Total Environment 476 (2014) 359-367.
[29] Z. Chen, S. Narayan, Z. Yang, and S. Rahman, An experimental investigation of hydraulic behaviour of fractures and joints in granitic rock. International Journal of Rock Mechanics and Mining Sciences 37 (2000) 1061-1071.
[30] T. Cladouhos, S. Petty, G. Foulger, B. Julian, and M. Fehler, Injection induced seismicity and geothermal energy. GRC Transactions 34 (2010) 1213-1220.
[31] O. Coussy, Mechanics of porous continua, Wiley, 1995.
[32] S.L. Crouch, and A. Starfield, Boundary element methods in solid mechanics: with applications in rock mechanics and geological engineering, Allen & Unwin, 1982.
[33] E.G. Daub, and J.M. Carlson, Friction, fracture, and earthquakes. Annual Review of Condensed Matter Physics 1 (2010) 397-418.
[34] R. Deb, and P. Jenny, Finite volume–based modeling of flow-induced shear failure along fracture manifolds. International Journal for Numerical and Analytical Methods in Geomechanics (2016).
[35] N. Deichmann, and D. Giardini, Earthquakes induced by the stimulation of an enhanced geothermal system below Basel (Switzerland). Seismological Research Letters 80 (2009) 784-798.
[36] J.H. Dieterich, Time-dependent friction and the mechanics of stick-slip. Pure and Applied Geophysics 116 (1978) 790-806.
[37] J.H. Dieterich, Modeling of rock friction: 1. Experimental results and constitutive equations. Journal of Geophysical Research 84 (1979) 2161.
[38] J.H. Dieterich, Earthquake nucleation on faults with rate and state-dependent strength. Tectonophysics 211 (1992) 115-134.
[39] L. Dorbath, N. Cuenot, A. Genter, and M. Frogneux, Seismic response of the fractured and faulted granite of Soultz-sous-Forêts (France) to 5 km deep massive water injections. Geophysical Journal International 177 (2009) 653-675.
[40] W.L. Ellsworth, Injection-induced earthquakes. Science 341 (2013) 1225942.

[41] K.F. Evans, A. Zappone, T. Kraft, N. Deichmann, and F. Moia, A survey of the induced seismic responses to fluid injection in geothermal and CO 2 reservoirs in Europe. Geothermics 41 (2012) 30-54.
[42] T. Garipov, M. Karimi-Fard, and H. Tchelepi, Discrete fracture model for coupled flow and geomechanics. Computational Geosciences 20 (2016) 149.
[43] E. Gaucher, M. Schoenball, O. Heidbach, A. Zang, P.A. Fokker, J.-D. van Wees, and T. Kohl, Induced seismicity in geothermal reservoirs: A review of forecasting approaches. Renewable and Sustainable Energy Reviews 52 (2015) 1473-1490.
[44] C. Geuzaine, and J.F. Remacle, Gmsh: A 3-D finite element mesh generator with built-in pre-and post-processing facilities. International Journal for Numerical Methods in Engineering 79 (2009) 1309-1331.
[45] A. Ghassemi, S. Tarasovs, and A.D. Cheng, Integral equation solution of heat extraction-induced thermal stress in enhanced geothermal reservoirs. International Journal for Numerical and Analytical Methods in Geomechanics 29 (2005) 829-844.
[46] S.J. Gibowicz, Seismicity induced by mining. Advances in Geophysics 32 (1990) 1-74.
[47] R.E. Goodman, Methods of geological engineering in discontinuous rocks, West Publication Company, New York, 1976.
[48] E. Gordeliy, R. Piccinin, J.A. Napier, and E. Detournay, Axisymmetric benchmark solutions in fracture mechanics. Engineering Fracture Mechanics 102 (2013) 348-357.
[49] M.A. Grant, J. Clearwater, J. Quinão, P.F. Bixley, and M. Le Brun, Thermal stimulation of geothermal wells: a review of field data, Thirty-Eighth Workshop on Geothermal Reservoir Engineering, Stanford, 2013.
[50] G. Grünthal, Induced seismicity related to geothermal projects versus natural tectonic earthquakes and other types of induced seismic events in Central Europe. Geothermics 52 (2014) 22-35.
[51] M.O. Häring, U. Schanz, F. Ladner, and B.C. Dyer, Characterisation of the Basel 1 enhanced geothermal system. Geothermics 37 (2008) 469-495.
[52] T. Hicks, R. Pine, J. Willis-Richards, S. Xu, A. Jupe, and N. Rodrigues, A hydro-thermo-mechanical numerical model for HDR geothermal reservoir evaluation. International Journal of Rock Mechanics and Mining Sciences & Geomechanics Abstracts 33 (1996) 499-511.
[53] A. Holland, Examination of possibly induced seismicity from hydraulic fracturing in the Eola Field, Garvin County, Oklahoma, Oklahoma Geological Survey, 2011.
[54] M. Hossain, M. Rahman, and S. Rahman, Hydraulic fracture initiation and propagation: roles of wellbore trajectory, perforation and stress regimes. Journal of Petroleum Science and Engineering 27 (2000) 129-149.
[55] IRENA, REthinking Energy 2017: Accelerating the global energy transformation, International Renewable Energy Agency, Abu Dhabi, 2017.
[56] F.D. Itasca, Fast lagrangian analysis of continua in 3 dimensions. Online Manual (2013).
[57] J.C. Jaeger, N.G. Cook, and R. Zimmerman, Fundamentals of rock mechanics, Blackwell Publishing Ltd, Malden, USA, 2007.
[58] P. Jeanne, J. Rutqvist, D. Vasco, J. Garcia, P.F. Dobson, M. Walters, C. Hartline, and A. Borgia, A 3D hydrogeological and geomechanical model of an Enhanced Geothermal System at The Geysers, California. Geothermics 51 (2014) 240-252.
[59] L. Jing, A review of techniques, advances and outstanding issues in numerical modelling for rock mechanics and rock engineering. International Journal of Rock Mechanics and Mining Sciences 40 (2003) 283-353.

[60] I. Johnston, G. Narsilio, and S. Colls, Emerging geothermal energy technologies. KSCE Journal of Civil Engineering 15 (2011) 643-653.
[61] M. Karimi-Fard, L.J. Durlofsky, and K. Aziz, An efficient discrete fracture model applicable for general purpose reservoir simulators. SPE Journal 9 (2003) 227-236.
[62] E. Keilegavlen, and J.M. Nordbotten, Finite volume methods for elasticity with weak symmetry. International Journal for Numerical Methods in Engineering 112 (2017) 939-962.
[63] G.E. King, Hydraulic fracturing 101: what every representative, environmentalist, regulator, reporter, investor, university researcher, neighbor, and engineer should know about hydraulic fracturing risk. Journal of Petroleum Technology 64 (2012) 34-42.
[64] G. Kloosterman, Contact methods in finite element simulations, University of Twente, 2002.
[65] T. Kohl, and T. Mégel, Predictive modeling of reservoir response to hydraulic stimulations at the European EGS site Soultz-sous-Forêts. International Journal of Rock Mechanics and Mining Sciences 44 (2007) 1118-1131.
[66] M. Kuna, Finite elements in fracture mechanics, Springer, 2013.
[67] K. Kuriyama, and Y. Mizuta, Three-dimensional elastic analysis by the displacement discontinuity method with boundary division into triangular leaf elements. International Journal of Rock Mechanics and Mining Sciences & Geomechanics Abstracts 30 (1993) 111-123.
[68] S.H. Lee, M. Lough, and C. Jensen, Hierarchical modeling of flow in naturally fractured formations with multiple length scales. Water Resources Research 37 (2001) 443-455.
[69] B. Legarth, E. Huenges, and G. Zimmermann, Hydraulic fracturing in a sedimentary geothermal reservoir: Results and implications. International Journal of Rock Mechanics and Mining Sciences 42 (2005) 1028-1041.
[70] K.A. Lie, An introduction to reservoir simulation using MATLAB. User guide for the MATLAB reservoir simulation toolbox (MRST), SINTEF ICT, Department of Applied Mathematics, 2016.
[71] K.A. Lie, S. Krogstad, I.S. Ligaarden, J.R. Natvig, H.M. Nilsen, and B. Skaflestad, Open-source MATLAB implementation of consistent discretisations on complex grids. Computational Geosciences 16 (2012) 297-322.
[72] Y.J. Liu, S. Mukherjee, N. Nishimura, M. Schanz, W. Ye, A. Sutradhar, E. Pan, N.A. Dumont, A. Frangi, and A. Saez, Recent advances and emerging applications of the boundary element method. Applied Mechanics Reviews 64 (2012) 030802.
[73] E.L. Majer, R. Baria, M. Stark, S. Oates, J. Bommer, B. Smith, and H. Asanuma, Induced seismicity associated with enhanced geothermal systems. Geothermics 36 (2007) 185-222.
[74] B. Matek, Annual US & global geothermal power production report, Geothermal Energy Association, 2016.
[75] H. Matsukawa, and T. Saito, Friction, stick-slip motion and earthquake, Modelling Critical and Catastrophic Phenomena in Geoscience, Springer, 2006, pp. 169-189.
[76] M.W. McClure, Generation of large postinjection-induced seismic events by backflow from dead-end faults and fractures. Geophysical Research Letters 42 (2015) 6647-6654.
[77] M.W. McClure, and R.N. Horne, Investigation of injection-induced seismicity using a coupled fluid flow and rate/state friction model. Geophysics 76 (2011) WC181-WC198.

[78] M.W. McClure, and R.N. Horne, Discrete fracture network modeling of hydraulic stimulation: Coupling flow and geomechanics, Springer Science & Business Media, 2013.
[79] M.W. McClure, and R.N. Horne, An investigation of stimulation mechanisms in Enhanced Geothermal Systems. International Journal of Rock Mechanics and Mining Sciences 72 (2014) 242-260.
[80] Y. Mukuhira, C. Dinske, H. Asanuma, T. Ito, and M. Häring, Pore pressure behavior at the shut-in phase and causality of large induced seismicity at Basel, Switzerland. Journal of Geophysical Research: Solid Earth 122 (2017) 411-435.
[81] H.D. Murphy, and M. Fehler, Hydraulic fracturing of jointed formations, International Meeting on Petroleum Engineering, Society of Petroleum Engineers, 1986.
[82] J. Napier, and D. Malan, A viscoplastic discontinuum model of time-dependent fracture and seismicity effects in brittle rock. International Journal of Rock Mechanics and Mining Sciences 34 (1997) 1075-1089.
[83] J.H. Norbeck, and R.N. Horne, Evidence for a transient hydromechanical and frictional faulting response during the 2011 Mw 5.6 Prague, Oklahoma earthquake sequence. Journal of Geophysical Research: Solid Earth (2016).
[84] J.M. Nordbotten, Cell-centered finite volume discretizations for deformable porous media. International Journal for Numerical Methods in Engineering 100 (2014) 399-418.
[85] J.M. Nordbotten, Convergence of a cell-centered finite volume discretization for linear elasticity. SIAM Journal on Numerical Analysis 53 (2015) 2605-2625.
[86] J.M. Nordbotten, Stable cell-centered finite volume discretization for Biot equations. SIAM Journal on Numerical Analysis 54 (2016) 942-968.
[87] P. Olasolo, M. Juárez, M. Morales, and I. Liarte, Enhanced geothermal systems (EGS): A review. Renewable and Sustainable Energy Reviews 56 (2016) 133-144.
[88] A.V. Phan, J.A.L. Napier, L.J. Gray, and T. Kaplan, Symmetric-Galerkin BEM simulation of fracture with frictional contact. International Journal for Numerical Methods in Engineering 57 (2003) 835-851.
[89] R. Pine, and A. Batchelor, Downward migration of shearing in jointed rock during hydraulic injections. International Journal of Rock Mechanics and Mining Sciences & Geomechanics Abstracts 21 (1984) 249-263.
[90] D. Pollard, and P. Segall, Theoretical displacements and stresses near fractures in rock: with applications to faults, joints, veins, dikes, and solution surfaces. Fracture mechanics of rock 277 (1987) 277-349.
[91] S. Portier, F.-D. Vuataz, P. Nami, B. Sanjuan, and A. Gérard, Chemical stimulation techniques for geothermal wells: experiments on the three-well EGS system at Soultz-sous-Forêts, France. Geothermics 38 (2009) 349-359.
[92] G. Preisig, E. Eberhardt, V. Gischig, V. Roche, M. Baan, B. Valley, P. Kaiser, D. Duff, and R. Lowther, Development of connected permeability in massive crystalline rocks through hydraulic fracture propagation and shearing accompanying fluid injection. Geofluids 15 (2015) 321-337.
[93] M. Rahman, M. Hossain, and S. Rahman, A shear-dilation-based model for evaluation of hydraulically stimulated naturally fractured reservoirs. International Journal for Numerical and Analytical Methods in Geomechanics 26 (2002) 469-497.
[94] C.E. Renshaw, On the relationship between mechanical and hydraulic apertures in rough-walled fractures. Journal of Geophysical Research: Solid Earth 100 (1995) 24629-24636.
[95] J.R. Rice, Spatio-temporal complexity of slip on a fault. Journal of Geophysical Research: Solid Earth 98 (1993) 9885-9907.

[96] A. Rocco, 2016 Geothermal Power: International Market Update, Geothermal Energy Association, 2016.
[97] E. Rothert, and S.A. Shapiro, Microseismic monitoring of borehole fluid injections: Data modeling and inversion for hydraulic properties of rocks, SEG Technical Program Expanded Abstracts 2002, Society of Exploration Geophysicists, 2002, pp. 1754-1757.
[98] A. Ruina, Slip instability and state variable friction laws. Journal of Geophysical Research: Solid Earth 88 (1983) 10359-10370.
[99] J. Rutqvist, and O. Stephansson, The role of hydromechanical coupling in fractured rock engineering. Hydrogeology Journal 11 (2003) 7-40.
[100] J. Ryder, Excess shear stress in the assessment of geologically hazardous situations. Journal of the Southern African Institute of Mining and Metallurgy 88 (1988) 27-39.
[101] T.H. Sandve, I. Berre, and J.M. Nordbotten, An efficient multi-point flux approximation method for discrete fracture–matrix simulations. Journal of Computational Physics 231 (2012) 3784-3800.
[102] J. Sausse, C. Dezayes, L. Dorbath, A. Genter, and J. Place, 3D model of fracture zones at Soultz-sous-Forêts based on geological data, image logs, induced microseismicity and vertical seismic profiles. Comptes Rendus Geoscience 342 (2010) 531-545.
[103] C.H. Scholz, Earthquakes and friction laws. Nature 391 (1998) 37-42.
[104] K. Shou, and S. Crouch, A higher order displacement discontinuity method for analysis of crack problems. International Journal of Rock Mechanics and Mining Sciences & Geomechanics Abstracts 32 (1995) 49-55.
[105] K.v. Terzaghi, The shearing resistance of saturated soils and the angle between the planes of shear, Proceedings of the 1st international conference on soil mechanics and foundation engineering, Harvard University Press Cambridge, MA, 1936, pp. 54-56.
[106] J.W. Tester, B.J. Anderson, A.S. Batchelor, D.D. Blackwell, R. DiPippo, E. Drake, J. Garnish, B. Livesay, M.C. Moore, and K. Nichols, The future of geothermal energy: Impact of enhanced geothermal systems (EGS) on the United States in the 21st century. Massachusetts Institute of Technology 209 (2006).
[107] D. Turcotte, and E. Oxburgh, Stress accumulation in the lithosphere. Tectonophysics 35 (1976) 183-199.
[108] T. Van Eck, F. Goutbeek, H. Haak, and B. Dost, Seismic hazard due to small-magnitude, shallow-source, induced earthquakes in The Netherlands. Engineering Geology 87 (2006) 105-121.
[109] J.B. Walsh, and W. Brace, The effect of pressure on porosity and the transport properties of rock. Journal of Geophysical Research: Solid Earth 89 (1984) 9425-9431.
[110] N. Warpinski, and L. Teufel, Influence of geologic discontinuities on hydraulic fracture propagation (includes associated papers 17011 and 17074). Journal of Petroleum Technology 39 (1987) 209-220.
[111] N.R. Warpinski, Hydraulic fracturing in tight, fissured media. Journal of Petroleum Technology 43 (1991) 146-209.
[112] B. Wassing, J. Van Wees, and P. Fokker, Coupled continuum modeling of fracture reactivation and induced seismicity during enhanced geothermal operations. Geothermics 52 (2014) 153-164.
[113] J. Willis-Richards, K. Watanabe, and H. Takahashi, Progress toward a stochastic rock mechanics model of engineered geothermal systems. Journal of Geophysical Research: Solid Earth 101 (1996) 17481-17496.

[114] P.A. Witherspoon, J.S. Wang, K. Iwai, and J.E. Gale, Validity of cubic law for fluid flow in a deformable rock fracture. Water Resources Research 16 (1980) 1016-1024.
[115] O.C. Zienkiewicz, R.L. Taylor, and J.Z. Zhu, Finite Element Method: Its basis and fundamentals., Elsevier, Incorporated, 2013.
[116] G. Zimmermann, and A. Reinicke, Hydraulic stimulation of a deep sandstone reservoir to develop an Enhanced Geothermal System: Laboratory and field experiments. Geothermics 39 (2010) 70-77.

Graphic design: Communication Division, UiB / Print: Skipnes Kommunikasjon AS

uib.no

ISBN: 978-82-308-3812-9